

**NASA  
Technical  
Memorandum**

**NASA TM - 100308**

**DISTRIBUTED CONTROL USING LINEAR MOMENTUM  
EXCHANGE DEVICES**

**By John P. Sharkey, Henry Waites, and  
George B. Doane III**

**Structures and Dynamics Laboratory  
Science and Engineering Directorate**

**October 1987**

**(NASA-TM-100308) DISTRIBUTED CONTROL USING  
LINEAR MOMENTUM EXCHANGE DEVICES (NASA) 50  
P Avail: NTIS AC A03/NP AC1 CSCL 228**

**187-24521**

**G3/18 0082689  
vaclas**



**National Aeronautics and  
Space Administration**

**George C. Marshall Space Flight Center**

## TECHNICAL MEMORANDUM

### DISTRIBUTED CONTROL USING LINEAR MOMENTUM EXCHANGE DEVICES

#### I. INTRODUCTION

This report documents Marshall Space Flight Center's (MSFC) role in the Air Force Wright Aeronautical Laboratory's (AFWAL) Vibration Control of Space Structures (VCOSS) experiment. This experiment, often referred to as VCOSS-II, was designed as a hardware demonstration stemming from the original VCOSS program which, in turn, was an outgrowth of AFWAL's Active Control of Space Structures (ACOSS) program. The purpose of ACOSS was to develop control strategies for Large Space Structures (LSS); VCOSS investigated the means to implement the ACOSS algorithms, while VCOSS-II concentrated on a hardware demonstration of VCOSS control elements. In particular, VCOSS-II was the active vibration suppression of an LSS test article by means of Linear Momentum Exchange Devices (LMEDs). Several LMEDs were to be strategically located on a generic LSS test structure to sense any vibratory motion of the structure and transfer the associated linear momentum to a proof mass using active control elements. The LMED controller, in turn, would dissipate the motion of the proof mass, thereby increasing the overall damping of the LSS test article.

Since NASA and the Air Force have mutual interests in the active control of LSS, the MSFC Ground Facility for Large Space Structures Control Verification (GF/LSSCV) was selected as the experimental site for VCOSS-II. AFWAL awarded a contract to the TRW Space and Technology Group to design, fabricate, deliver and demonstrate LMED hardware on the GF/LSSCV. A thirteen meter ASTROMAST with an 8-in. triangular cross-section was selected as the test article. This lightweight, flexible beam, which was formerly a spare magnetometer boom for the Voyager space-craft, has previously been used at MSFC for LSS control experiments. The beam is attached vertically to a three degree of freedom, flight quality pointing mount, with two complete Inertial Reference Units (IRUs) attached one to either end of the beam. The LMEDs were designed to complement this assortment of control hardware. Planning included hardware demonstrations of the LMEDs alone and in conjunction with the GF/LSSCV three gimbal pointing mount.

The original VCOSS-II test plan was arranged along the following lines. MSFC agreed to provide the test facility, perform preliminary modal tests on the test article and provide mechanical integration support for the experiments. MSFC agreed also to provide an independent preliminary structural dynamic model verified by the modal tests. In exchange for the use of the GF/LSSCV, AFWAL granted MSFC unrestricted use of the VCOSS-II hardware for an indefinite period to perform independent control studies, provided that these studies did not interfere with the VCOSS program schedule.

This report will address the MSFC control experiments. A brief description of the facility, control hardware and test configuration is followed by a summary of dynamic models of the structure and of the LMEDs. This will be followed by a description of the MSFC control strategies. Experimental results are then presented. A brief section of conclusions and recommendations appears at the end of the report. It should be stressed that this report is intended to document the MSFC work to date,

and not to provide a comprehensive analysis of the applicability of LMEDs for LSS. The work to be presented reflects a status report of the initial testing performed through early 1986. Experimental work with the LMEDs is continuing, the results of which will be published in future reports.

## II. EXPERIMENT DESCRIPTION

This section will describe the experimental facility, the hardware components and the experimental configurations. Dynamic models of each configuration developed by the Control Dynamics Company for MSFC will be discussed. Analytic models of the basic LMED components will also be discussed.

### 2.1 Experimental Facilities

#### 2.1.1 GF/LSSCV

Figure 1 outlines the basic components of the LSS test article in the GF/LSSCV. The ASTROMAST is shown suspended vertically from a modified version of the Sperry Corporation's engineering model of the Advanced Gimbal System (AGS). The AGS consists of two gimballed dc torque motors capable of developing 51 Newton meters (N-m). The AGS is mounted below an air bearing about the vertical axis with a 19 N-m torque motor. All three torque motors have measured bandwidths in excess of 100 Hz. The modified AGS is attached to a hydraulically driven, two translational degree of freedom, Base Excitation Table (BET). A three-axis accelerometer unit is located on the BET, and an identical accelerometer unit is located on the tip sensor package (at ground level). These accelerometers have digital outputs, 25 Hz bandwidth and 11 micro-g sensitivity. Three single axis rate gyros are attached to the AGS mounting plate. These gyros have 40 Hz bandwidths, 2 arc-second/second sensitivity, one degree per second saturation limits, and provide analog output voltages. The tip rate gyros have 70 Hz bandwidths, digital outputs, and 50 to 90 arc-second/second sensitivity. A MSFC built COSMEC computer performs the Input/Output (I/O) task of interfacing the sensors and actuators with a HP-9000 control computer. The HP-9000 and COSMEC are currently configured to operate at a 50 Hz sample rate. The HP-9000 performs digital sensor indication updates, coordinate transformations, IRU functions and control law implementation, all of which is accomplished in the HP BASIC language. The ASTROMAST is 13 m long with a 20.3 cm on a side equilateral triangular cross-section and three continuous S-glass longerons. There are 92 flexible battens distributed horizontally along the beam in 14.3 cm increments. These locations will be referenced as station numbers with station 1 at the AGS mounting plate and station 92 at the tip. The ASTROMAST has a static twist of 260 deg about the vertical axis when loaded as in this configuration. Figure 2 is a photograph of the Astromast in a previous experimental configuration. A 4-m cruciform is shown attached to the tip sensor package.

#### 2.1.2 Linear Momentum Exchange Device

Two pairs of LMEDs are identified in representative locations in Figure 1. Figure 3 is a close-up photograph of one such LMED pair mounted to the ASTROMAST. The schematic drawing in Figure 4 identifies the major components. Two LMEDs are shown mounted orthogonally to each other on opposite sides of a rigid aluminum frame

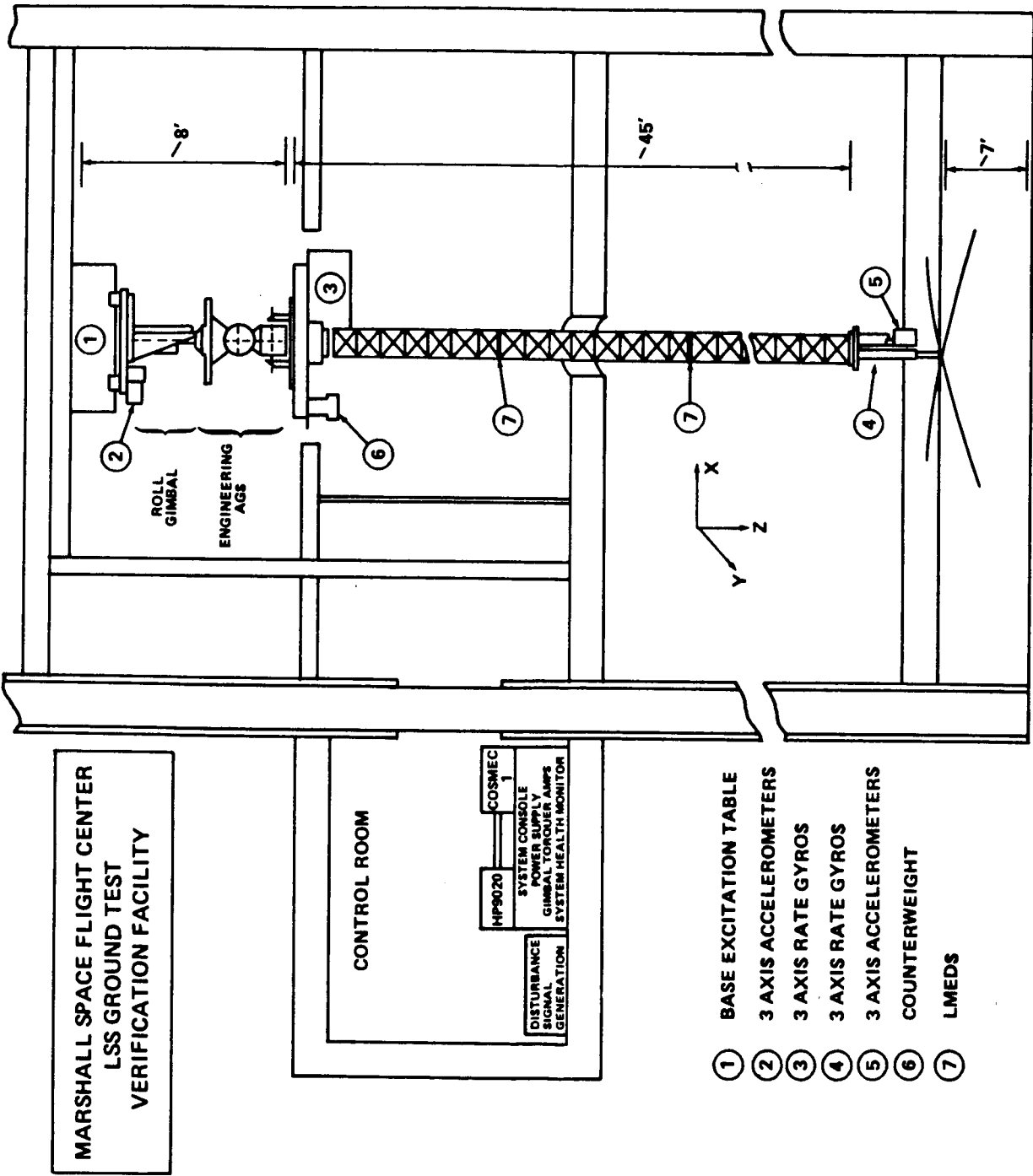


Figure 1. MSFC LSS Ground Test Verification Facility.

ORIGINAL PAGE IS  
OF POOR QUALITY

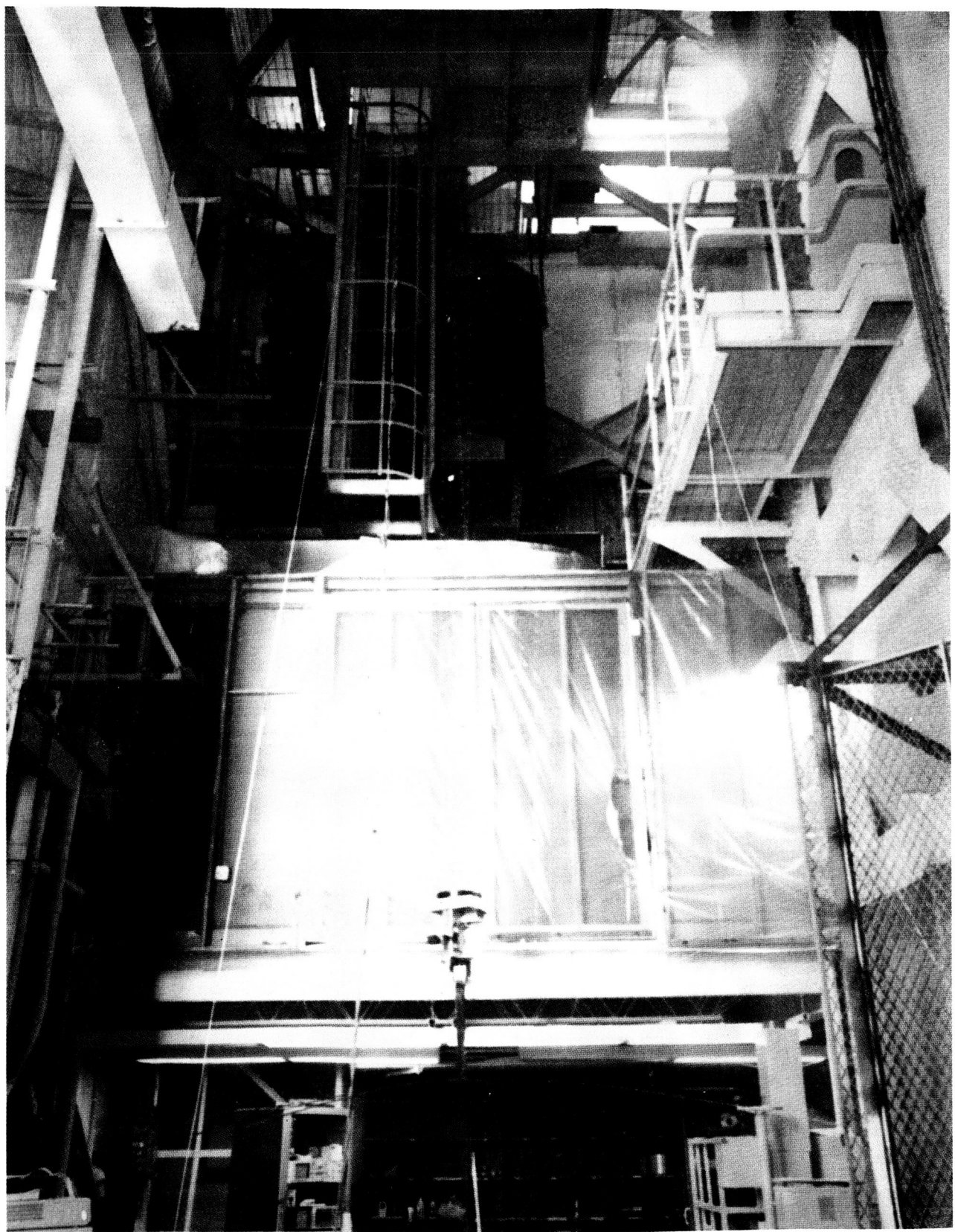


Figure 2. Photograph of GF/LSSCV ASTROMAST.

ORIGINAL PAGE IS  
OF POOR QUALITY

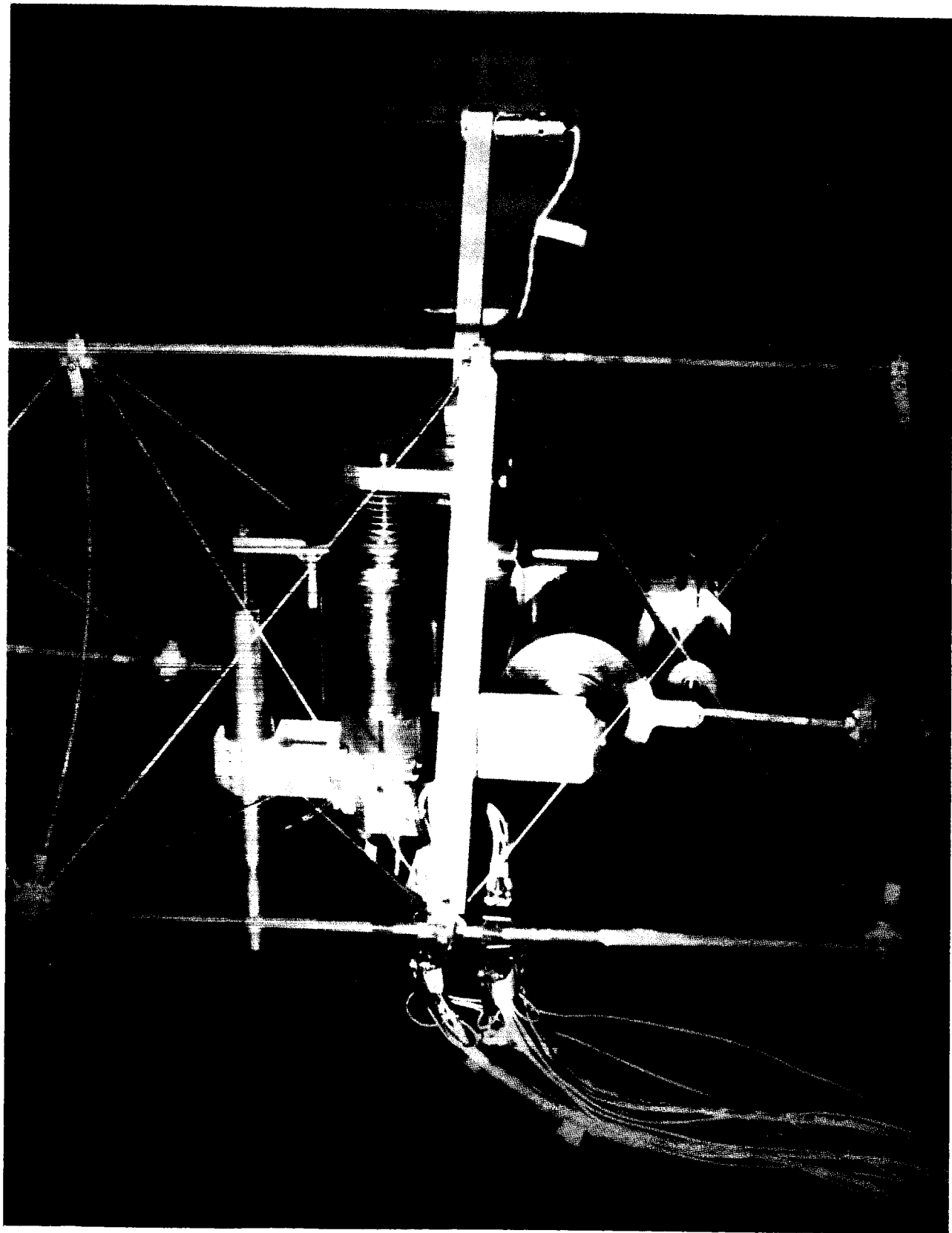


Figure 3. Close-up photograph of LMED mounted on ASTROMAST.

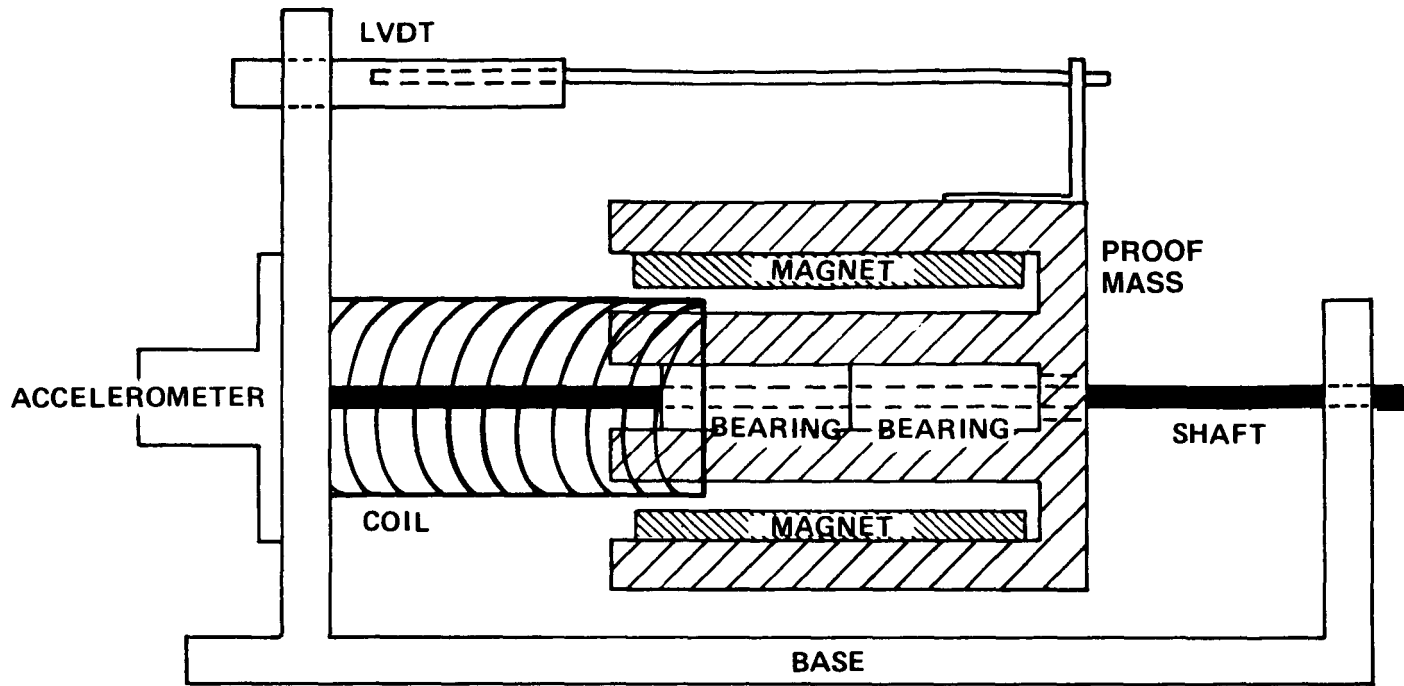


Figure 4. Schematic drawing of LMED construction.

which substitutes for one of the ASTROMAST flexible battens. Each LMED consists of a 0.75 Kg cylindrical moving mass with  $\pm 1.27$  cm of linear travel along a stainless steel shaft; a dc coupled, electronically driven voice coil attached to the frame; a Linear Variable Displacement Transducer (LVDT) which measures the position of the proof-mass relative to the frame; and a linear accelerometer with a pre-amplifier stage. The input axis of the accelerometer is aligned with the stainless steel shaft. The proof-mass contains samarium cobalt permanent magnets which move outside of the actuating coils, and stainless steel ball bearings which support the moving mass internally. The LVDT core is teflon coated, and its attachment to the moving mass restricts rotational motion. The moving masses of the two LMEDs are placed at the centroid of the triangular frame. The total non-moving mass of the LMED pair is 1.0 Kg which gives a total mass of 2.5 Kg for a complete pair of devices. As an option, each LMED can employ centering springs on either side of the proof-mass. Figure 3 also shows laser diode sources mounted on "diving board" extensions. These lasers are part of an optical position sensing system which was not used in VCOSS-II, and will not be discussed in this report.

## 2.2 Experimental Configuration

The VCOSS experiment ultimately involved three test configurations as shown schematically in Figure 5. In the first configuration identified as configuration 1-A, the AGS and BET were rigidly constrained and the 18-Kg tip sensor package was removed. The two LMED pairs were located at stations 91 and 49. These locations were selected for the following reasons. The middle LMEDs, which were labelled A and B, would have control authority throughout the first 20 bending modes, especially at the mid-frequency modes. The lower pair of actuators would have control authority over the first eleven bending modes, primarily at lower frequencies. In addition, the 42 station separation corresponds to 120 deg of twist of the ASTROMAST.

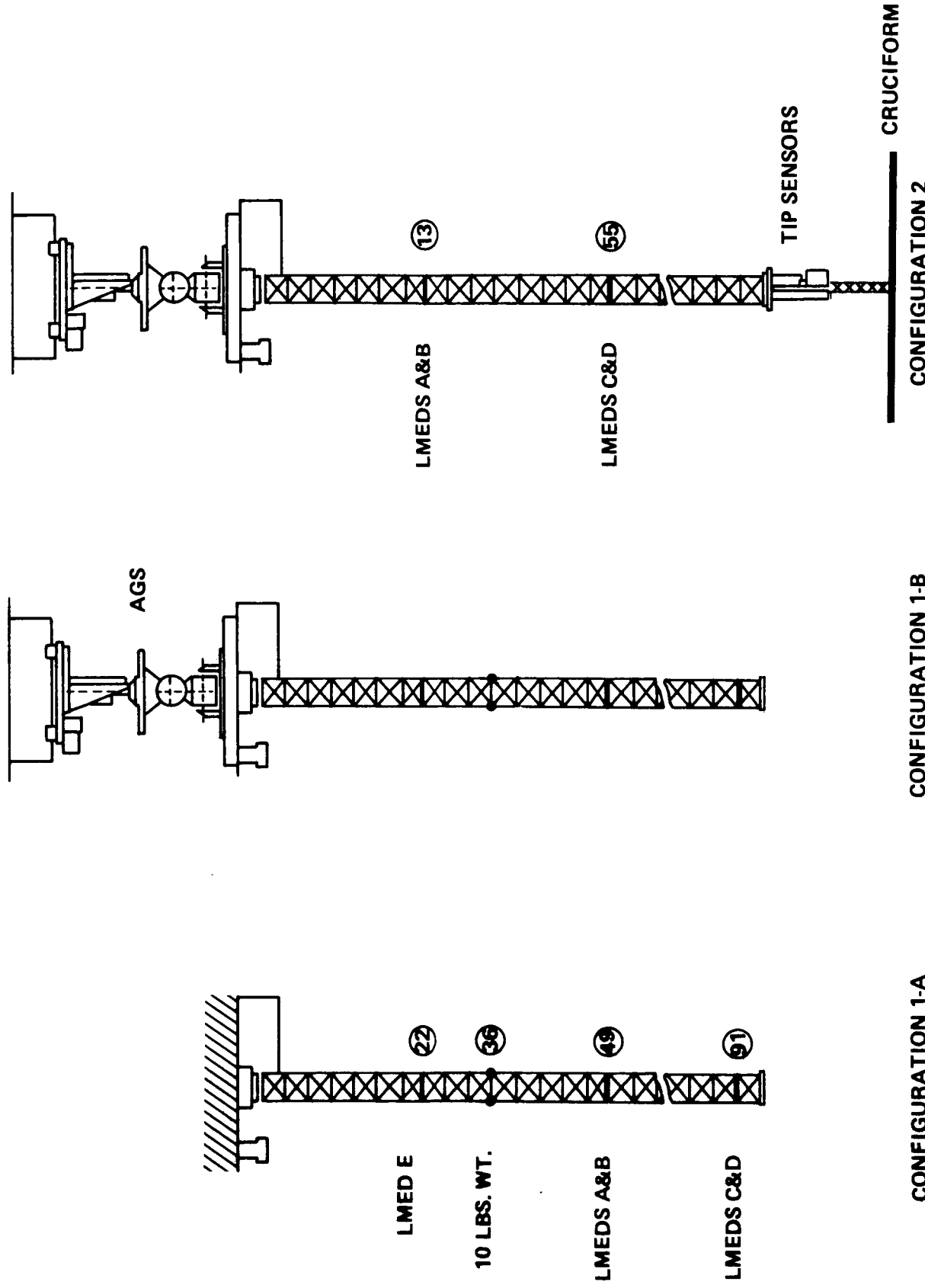


Figure 5. Schematic of the VCOSS-II test configurations.

Since the LMED frame is an equilateral triangle, the middle device could be reoriented by 120 deg to align it with the lower device. The discrete possibilities for mounting these devices implies a 60 deg (21 station) separation intended for best alignments; 30 deg intervals will introduce  $\pm 1.4$  deg offsets. A spare LMED (a misnomer, since this device lacks an accelerometer) was located at station 22 to serve as an excitation source. This device, labelled LMED-E, was oriented about 43 deg relative to the other actuators. To prevent the relatively massive actuators from creating mid-frequency vibration nodes on the structure, three 1.55 Kg lumped masses were attached to the structure (one each longeron) at station 36.

Configuration 1-A, described above, allowed the LMEDs to be tested independent of the AGS system, thereby simplifying the modeling task. Configuration 1-B is similar to 1-A except that the AGS system was free to rotate, which caused the frequencies of vibration to decrease. In configuration 2, the tip sensor package was mounted to the ASTROMAST along with a 3.6 Kg aluminum cruciform, with four approximately 2-m long, constant cross-section (0.635 cm) arms. This had the combined effect of further decreasing the modal frequencies while increasing the modal density, and coupling the bending and torsion modes. The excitation source, LMED-E, was removed along with the three lumped masses. The middle pair of actuators, LMEDs A and B, were located at station 13 and the lower pair at station 55. The BET was unlocked and could serve as the excitation source, as could the AGS torquers.

The three configurations represent a departure from the original test plan. Configuration 1-A was planned as the baseline to demonstrate and characterize the LMED hardware components. The addition of the aluminum cruciform to the configuration was planned to demonstrate the robustness of the controller. Finally, the AGS gimbals were to be unlocked and actively driven along with the LMEDs to demonstrate multiple input/multiple output control techniques. As it turned out, configurations 1-A and 1-B were used to test an analog controller. Configuration 1-B was also used to demonstrate the MSFC designed digital control of the LMEDs. Configuration 2 was used for a demonstration of the simultaneous use of the AGS torque motors and the LMED systems for control. This selection of test configurations was dictated by schedule constraints which, combined with GF/LSSCV hardware problems, required unrestricted access to the system components for troubleshooting and testing.

### 2.3 Structural Dynamic Models

MSFC and the Control Dynamics Company spent a considerable amount of time generating structural dynamic models of the planned VCOSS test configurations and verifying these models with extensive modal tests on the structure. However, the last minute changes in these configurations (as described in the previous section) meant that the corresponding changes to the dynamic models could not be verified by modal tests. Thus, the models to be presented herein provide reasonable levels of accuracy, but not necessarily the best that could be achieved given full experimental information.

Figure 6 depicts the elements used to model test configuration 1-A. The local coordinate frames associated with each element define the numerical degrees of freedom of the overall structure. The first index along an axis indicates a translational degree of freedom; the second index indicates a rotational degree of freedom. The analysis was performed with the ISMIS (Interactive Structures and Matrix Interpretive System) finite element code. This model contains 41 degrees of freedom including the five moving masses associated with the five LMEDs. The LMED models also

included centering springs which produced a set of five nested modes near 1 Hz. Table 1 provides the frequencies and the mode shapes at each device. For example, LMED-E exerts a force on the moving mass at degree of freedom number 37; the components of an equal and opposite force are applied to the structure at locations 7 and 8. Torsional modes in this model, which is highly symmetric, are evident in Table 1 by the mode with zero lateral displacements, i.e., modes 10, 13, 18, 19, 20, 23, and 24. These modes can be neglected in subsequent analyses since they do not interact with the LMEDs in this model. The last column on the right identifies the frequencies of vibration which were evident in the open loop frequency response data presented in Section IV. Figure 7 and Table 2 provide the analogous information for configuration 1-B; Figure 8 and Table 3 apply to configuration 2.

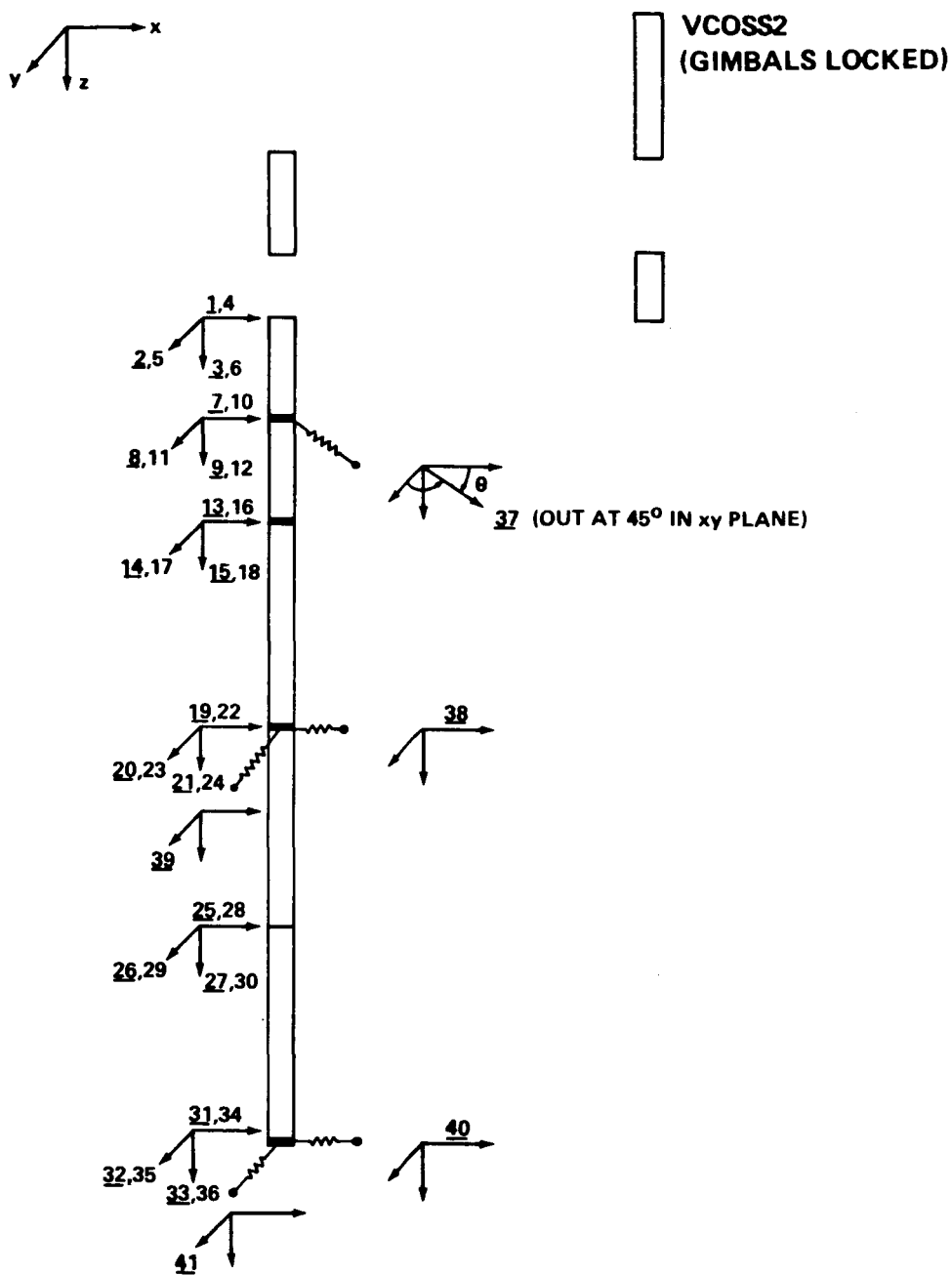


Figure 6. Dynamic model of configuration 1-A.

TABLE 1. VCOSS-II DYNAMIC MODEL FOR CONFIGURATION 1-A  
(AGS Gimbals Locked; No Tip Sensors or Cruciform)

MODE	FREQ (Hz)	DAMP ( $\zeta$ )	$\Phi_7$	$\Phi_8$	$\Phi_9$	$\Phi_{20}$	$\Phi_{31}$	$\Phi_{32}$	$\Phi_{37}$	$\Phi_{38}$	$\Phi_{39}$	$\Phi_{40}$	$\Phi_{41}$	DESCRIPTION	FREQUENCY (Hz) MEASURED	
			AccA	AccB	AccC	AccD	LMED-E	LMED-A	LMED-B	LMED-C	LMED-D					
1	0.311	0.005	.342	.342	1.176	1.176	3.418	3.418	.531	1.292	1.292	3.754	3.754	1st bending +X+y	0.30	
2	0.311	0.005	.342	.342	1.176	-1.176	3.418	-3.418	0.0	1.292	-1.292	3.755	-3.754	1st bending +X-y	0.30	
3	0.905	0.005	.684	.684	1.269	1.269	-.726	-.726	3.991	5.239	5.239	-2.998	-2.998	2nd bending	0.95	
4	0.917	0.005	.671	.671	1.300	-1.300	-.692	-.692	0.0	5.839	-5.839	-3.116	3.116	2nd bending	-	
5	1.033	0.005	.086	.086	-.043	-.043	.006	.006	9.610	-.3.395	-.3.395	0.499	0.499	LMED	1.10	
6	1.181	0.005	.541	.541	-1.213	1.213	-1.419	1.419	0.0	4.174	-4.174	4.882	-4.882	LMED	-	
7	1.191	0.005	.437	.437	1.112	1.112	1.635	1.635	-1.967	-3.547	-3.547	-5.215	-5.215	LMED	1.14	
8	1.384	0.005	-1.110	1.110	-1.692	1.692	2.488	-2.488	0.0	2.187	-2.187	-3.215	3.215	LMED	-	
9	1.418	0.005	-1.139	-1.139	-1.877	-1.877	2.353	2.353	1.868	2.177	2.177	-2.728	-2.728	LMED	1.32	
10	2.496	0.005	0.0	0.0	0.0	0.0	0.0	0.0	0.0	0.0	0.0	0.0	0.0	1st torsion	-	
11	4.642	0.005	2.537	-2.537	-2.300	2.300	1.047	1.047	0.0	0.121	-0.121	-0.055	0.055	3rd bending	3.3	
12	4.926	0.005	-2.568	-2.568	2.199	2.199	-1.064	-1.064	0.169	-0.102	-0.102	0.049	0.049	3rd bending	4.92	
13	7.309	0.005	0.0	0.0	0.0	0.0	0.0	0.0	0.0	0.0	0.0	0.0	0.0	2nd torsion	-	
14	9.919	0.005	3.099	-3.099	-1.508	1.508	-.891	-.891	0.0	.017	-.017	.010	-.010	4th bending	8.12	
15	10.838	0.005	3.107	-3.107	-2.200	-2.200	-.930	-.930	0.0	.020	.020	.008	.008	4th bending	9.28	
16	14.414	0.005	-3.071	3.071	-2.084	2.084	-.500	-.500	-.041	-.011	-.011	.003	-.003	5th bending	11.3	
17	16.939	0.005	5.823	5.823	1.362	1.362	.301	.301	-.031	-.005	-.005	-.001	-.001	5th bending	12.08	
18	19.470	0.005	0.0	0.0	0.0	0.0	0.0	0.0	0.0	0.0	0.0	0.0	0.0	0.0	0.0	
19	22.041	0.005	0.0	0.0	0.0	0.0	0.0	0.0	0.0	0.0	0.0	0.0	0.0	0.0	0.0	
20	25.438	0.005	0.0	0.0	0.0	0.0	0.0	0.0	0.0	0.0	0.0	0.0	0.0	0.0	0.0	
21	34.667	0.005	0.236	-.236	1.167	-1.167	-.720	-.720	0.0	-.001	.001	.001	-.001	-.001	0.0	0.0
22	34.702	0.005	-.491	-1.172	-1.172	-.719	.719	.001	.001	.001	.001	-.001	-.001	0.0	0.0	0.0
23	35.323	0.005	0.0	0.0	0.0	0.0	0.0	0.0	0.0	0.0	0.0	0.0	0.0	0.0	0.0	0.0
24	46.204	0.005	0.0	0.0	0.0	0.0	0.0	0.0	0.0	0.0	0.0	0.0	0.0	0.0	0.0	0.0

Extracted from Control Dynamics Company ISMIS model

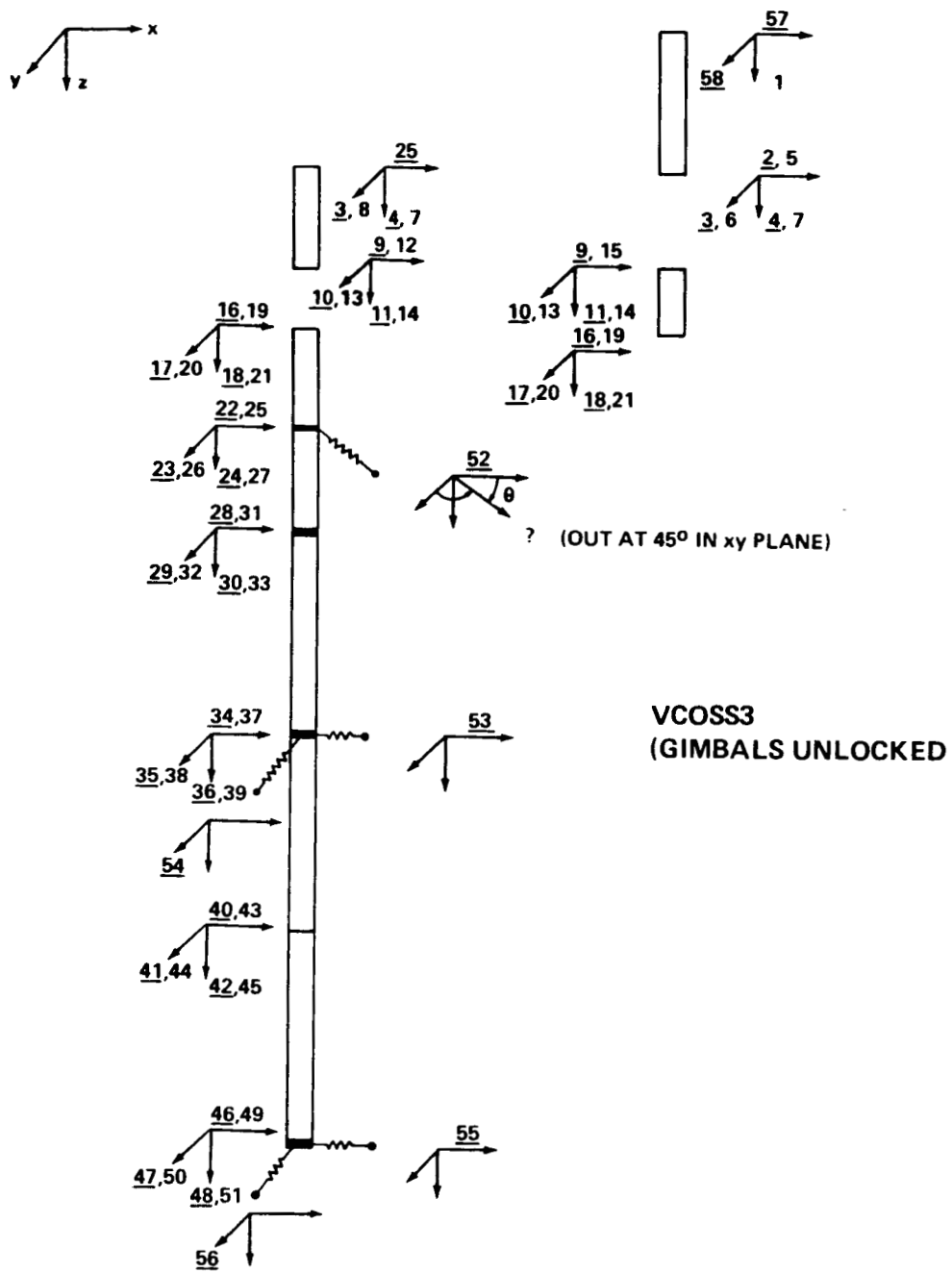


Figure 7. Dynamic model of configuration 1-B.

TABLE 2. VCROSS-II DYNAMIC MODEL FOR CONFIGURATION 1-B  
(Gimbals Unlocked; No Tip Sensors or Cruciform)

MODE	FREQ (Hz)	DAMP ( $\zeta$ )	$\Phi_{22}$	$\Phi_{23}$	$\Phi_{34}$	$\Phi_{35}$	$\Phi_{46}$	$\Phi_{47}$	$\Phi_{52}$	$\Phi_{53}$	$\Phi_{54}$	$\Phi_{55}$	$\Phi_{56}$	DESCRIPTION	FREQUENCY (Hz) MEASURED
			AccA	AccB	AccC	AccD		LMED-E	LMED-A	LMED-B	LMED-C	LMED-D			
1	0.0	0.0	0.0	0.0	0.0	0.0	0.0	0.0	0.0	0.0	0.0	0.0	0.0	Z rotation	-
2	0.0	0.0	0.383	-0.007	-0.383	-0.009	0.383	-0.009	0.265	0.383	-0.009	-0.383	-0.009	X translation	-
3	0.0	0.0	-0.009	-0.352	-0.009	-0.352	-0.009	-0.352	-0.255	-0.009	-0.352	-0.009	-0.352	Y translation	-
4	0.236	0.003	0.985	0.005	2.091	0.011	4.403	0.736	0.006	2.204	0.012	4.642	0.012	1st Y bending	-
5	0.244	0.003	2.053	-0.006	4.415	-0.014	7.111	2.172	-0.007	4.672	-0.014	1st X bending	-	1st X bending	-
6	0.750	1.536	0.947	1.745	1.091	-1.933	-1.222	3.663	3.643	2.277	-4.036	-2.551	2nd bending (?)	2nd bending (?)	-
7	0.764	1.012	-1.565	1.177	-1.847	-1.222	1.934	-0.851	2.560	-4.017	-2.658	4.217	4.217	2nd bending (?)	2nd bending (?)
8	1.028	0.132	0.121	-0.096	-0.092	-0.017	0.017	8.580	-4.610	-4.426	811	811	811	LMED-E	1.05
9	1.115	-0.904	0.803	-1.041	0.951	-0.247	0.232	-0.471	6.896	-6.301	1.634	-1.534	-1.534	LMED-A	1.07
10	1.156	-0.721	0.814	1.073	1.243	0.684	0.804	4.581	-4.530	-5.247	-2.247	-3.394	-3.394	LMED-B	1.4
11	1.265	-0.816	0.527	-0.378	0.243	3.189	-2.172	4.24	0.785	-5.505	-6.628	4.515	4.515	LMED-C	1.4
12	1.287	-0.722	-1.054	-0.567	-0.843	2.067	3.166	2.166	1.061	1.578	-3.870	-5.927	-5.927	LMED-D	1.4
13	2.510	3.387	-2.411	-1.855	1.408	-0.986	0.746	-0.007	0.020	-0.015	0.010	-0.008	-0.008	3rd bending X	1.96
14	2.751	2.575	3.062	-2.007	-2.489	-0.813	-1.006	-0.036	0.018	-0.023	0.007	0.009	0.009	3rd bending Y	2.78
15	3.679	-3.969	2.962	-2.097	1.900	-0.498	0.451	-0.001	0.001	-0.010	-0.003	-0.002	-0.002	4th bending	4.6
16	5.117	5.701	6.003	1.239	1.328	0.274	0.294	-0.030	-0.005	-0.005	-0.001	-0.001	-0.001	4th bending	4.9
17	6.003	0.0	0.0	0.0	0.0	0.0	0.0	0.0	0.0	0.0	0.0	0.0	0.0	1st torsion	-
18	7.309	0.0	0.0	0.0	0.0	0.0	0.0	0.0	0.0	0.0	0.0	0.0	0.0	2nd torsion	-
19	10.161	3.387	-2.411	-1.855	1.408	-0.986	0.746	-0.007	0.020	-0.015	0.010	-0.008	-0.008	5th bending	11.78
20	10.978	2.575	3.062	-2.007	-2.489	-0.813	-1.006	-0.036	0.018	0.023	0.007	-0.009	-0.009	5th bending	12.28
21	14.578	-3.369	2.962	-2.097	1.900	-0.498	0.451	-0.001	0.011	-0.010	-0.003	-0.002	-0.002	6th bending	-
22	17.231	5.701	6.003	1.239	1.328	0.274	0.294	-0.030	-0.005	-0.005	-0.001	-0.001	-0.001	6th bending	-
23	19.450	0.0	0.0	0.0	0.0	0.0	0.0	0.0	0.0	0.0	0.0	0.0	0.0	3rd torsion	-
24	22.041	0.0	0.0	0.0	0.0	0.0	0.0	0.0	0.0	0.0	0.0	0.0	0.0	4th torsion	-
25	25.441	0.0	0.0	0.0	0.0	0.0	0.0	0.0	0.0	0.0	0.0	0.0	0.0	5th torsion	-

Note: Generalized mass of one for all modes

**TRANSLATION, ROTATION**

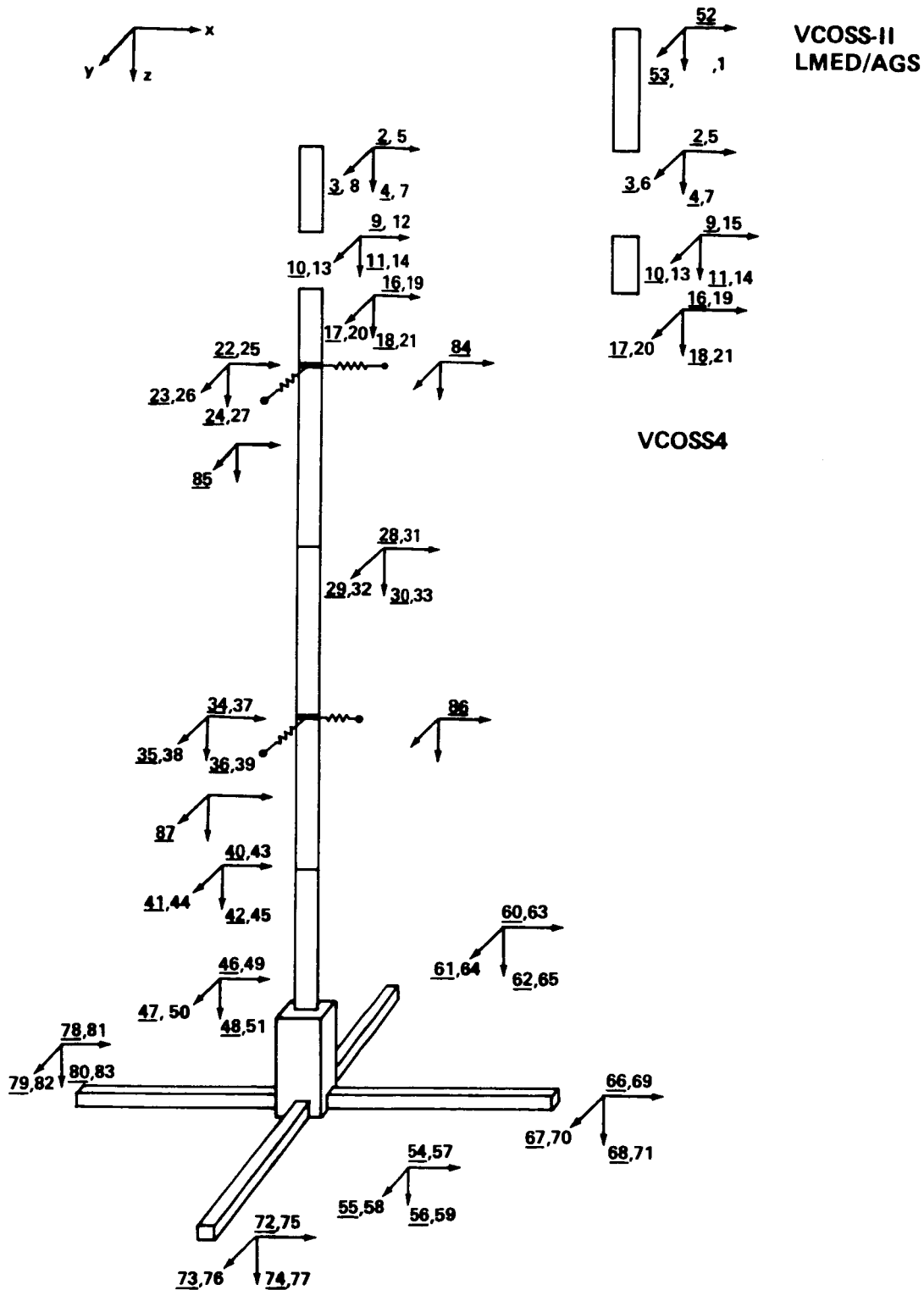


Figure 8. Dynamic model of configuration 2.

TABLE 3. VCOSS-II DYNAMIC MODEL FOR CONFIGURATION 2

MODE	FREQ (Hz)	$\Phi_1$ $T_z$	$\Phi_8$ $T_y$	$\Phi_{15}$ $T_x$	$\Phi_{22}$ $A_{CC}$	$\Phi_{23}$ $A_{CCB}$	$\Phi_{34}$ $A_{CC}$	$\Phi_{35}$ $A_{CCD}$	$\Phi_{84}$ $LMED-A$	$\Phi_{85}$ $LMED-B$	$\Phi_{86}$ $LMED-C$	$\Phi_{87}$ $LMED-D$	DESCRIPTION	FREQUENCY MEASURED	NO MEASURED DATA
1	0.00	.221	0.0	0.0	0.0	0.0	0.0	0.0	0.0	0.0	0.0	0.0	0.0	TORSION	
2	0.00	0.0	0.0	0.0	.038	0.0	.038	0.0	.038	0.0	.038	0.0	.038	X-BENDING	
3	0.00	0.0	0.0	0.0	.035	0.0	.035	0.0	.035	0.0	.035	0.0	.035	Y-BENDING	
4	0.142	0.0	0.0	-.015	0.0	.021	0.0	-.116	0.0	.020	0.0	-.117	0.0	Y-BENDING	
5	0.146	0.0	-.013	0.0	-.020	0.0	-.114	0.0	-.001	0.0	0.0	-.001	0.0	X-BENDING	
6	0.356	-.064	0.0	0.0	0.0	0.0	0.0	0.0	0.0	0.0	0.0	0.0	0.0	TORSION	
7	0.900	0.0	.047	0.0	.086	0.0	.174	0.0	.456	-.001	.917	-.001	.001	X-BENDING	
8	0.914	0.0	0.0	-.041	0.0	.070	0.0	.161	.001	.427	.001	.978	.001	Y-BENDING	
9	0.994	0.0	.009	0.0	.013	0.0	-.007	0.0	1.031	-.001	-.519	0.0	0.0	X-LMEDS	
10	0.995	0.0	0.0	-.008	0.0	.011	0.0	-.005	.001	1.060	0.0	0.0	0.0	Y-LMEDS	
11	1.123	0.0	0.0	.006	0.0	-.011	0.0	-.034	0.0	.043	-.001	.130	LEG # 1		
12	1.153	0.0	.008	.002	.014	-.003	.035	-.010	-.042	.009	-.107	.030	LEGS # 1 & 2		
13	1.175	0.0	.014	0.0	.025	.001	.056	.003	-.066	-.002	-.147	-.007	LEG # 2		
14	1.216	0.0	-.010	.007	-.019	-.012	-.042	-.034	.039	-.024	.088	.070	LEGS # 2 & 3		
15	1.234	0.0	-.002	-.011	-.003	-.020	-.007	.053	.007	-.038	.014	.101	LEG # 3		
16	1.281	0.0	-.023	-.009	-.041	.015	-.078	.041	.063	-.023	.122	.064	LEGS # 3 & 4		
17	1.289	0.0	-.034	.004	-.060	-.006	-.112	-.017	.091	.010	.170	.026	LEGS 3 & 4		
18	1.367	0.0	.105	0.0	.182	.001	.304	.002	-.209	-.001	.350	-.002	LEG # 4		
19	1.518	0.0	0.0	-.120	0.0	.203	0.0	.445	0.0	-.156	0.0	0.0	0.0	Y-BENDING	
20	2.649	0.0	-.136	0.0	-.141	0.0	.390	0.0	.023	0.0	-.065	0.0	0.0	X-BENDING	
21	3.053	-.006	-.001	-.001	-.001	.002	.003	0.0	0.0	0.0	0.0	0.0	0.0	TORSION	
22	3.599	0.0	0.0	-.263	0.0	.325	0.0	-.258	0.0	-.027	0.0	0.0	0.0	Y-BENDING	
23	4.412	.006	0.0	.001	0.0	-.001	.001	0.0	0.0	0.0	0.0	0.0	0.0	TORSION	
24	6.282	0.0	-.042	0.0	.092	0.0	.190	0.0	-.002	0.0	-.005	0.0	0.0	X-BENDING	
25	6.604	0.0	0.0	-.113	0.0	.030	0.0	-.231	0.0	-.001	0.0	0.0	0.0	Y-BENDING	
26	7.220	-.007	0.0	0.0	0.0	0.0	0.0	0.0	0.0	0.0	0.0	0.0	0.0	TORSION	
27	9.917	0.0	-.069	0.0	.427	0.0	-.214	0.0	-.004	0.0	0.0	0.002	0.0	LEGS # 1, 2, 3, 4	
28	10.610	0.0	.001	-.008	-.004	-.009	.003	.004	0.0	0.0	0.0	0.0	0.0	LEGS # 1, 2, 3	
29	11.112	0.0	0	.192	0.0	.270	0.0	-.149	0.0	-.002	0.0	0.0	0.001	LEG # 1	
30	11.250	0.0	-.001	.104	.008	.152	-.006	-.087	0.0	-.001	0.0	0.0	0.0	LEGS # 1	
31	11.282	0.0	.003	.043	-.021	.064	.014	-.037	0.0	-.001	0.0	0.0	0.0	LEGS # 1	
32	11.726	0.0	.002	.006	-.018	.010	.012	-.006	0.0	0.0	0.0	0.0	0.0	LEGS # 2	
33	11.868	0.0	.001	-.018	-.011	-.031	.007	.021	0.0	0.0	0.0	0.0	0.0	LEGS # 2	
34	12.285	0.0	0.0	.011	.003	.020	-.002	-.014	0.0	0.0	0.0	0.0	0.0	LEGS # 3	
35	12.478	0.0	-.001	-.001	-.008	.009	-.015	-.006	.010	0.0	0.0	0.0	0.0	LEGS # 3	
36	12.893	0.0	.001	0.0	-.012	.001	.008	-.001	0.0	0.0	0.0	0.0	0.0	LEGS # 4	
37	13.298	0.0	0.0	.004	.002	.009	-.001	-.006	0.0	0.0	0.0	0.0	0.0	TORSION	
38	18.919	0.0	.026	0.0	-.384	0.0	-.048	0.0	.001	0.0	0.0	0.0	0.0	X-BENDING	
39	19.252	0.0	0.0	-.095	0.0	-.386	0.0	-.040	0.0	0.0	0.0	0.0	0.0	Y-BENDING	
40	20.197	0.0	0.0	0.0	0.0	0.0	0.0	0.0	0.0	0.0	0.0	0.0	0.0	TORSION	

## 2.4 LMED Analysis and Modeling

This section will describe a limited dynamic model of the LMED including analysis of the linear motor drive electronics, actuator dynamics, the accelerometer and accelerometer preamplifier, and the LVDT relative position sensor. The model is developed analytically and supported with laboratory measurements. A high fidelity model suitable for computer simulation was not completed due to the complexity and magnitude of the measured non-linearities. The level of influence of these non-linearities over the actuator dynamics was later greatly diminished by techniques developed in the MSFC laboratories in conjunction with Control Dynamics Company.

Figure 9 provides a transfer function description of the major LMED components. This model represents a single device as tested on a laboratory bench, for example, on an ideal air bearing, i.e., "slippery plate." The forward path describes the input/output relationship with respect to the experiment control computer;  $V_{cmd}$  is the command voltage from the controller and  $V_a$  is the return signal from the accelerometer preamplifier. The feedback path describes the dynamics of the motion of the "proof mass"  $M_p$ , incorporating viscous damping and centering springs. The sum of these feedback return forces with that produced by the motor's solenoid coil is applied in an equal but opposite manner to the proof mass and the actuator base. The following parameters are identified in the model.

$K_D = 0.2 \text{ (A/V)}$  the frequency independent gain of the driver electronics

$\tau_1 = 2 \times 10^{-4} \text{ (sec)}$

$\tau_2 = 4 \times 10^{-5} \text{ (sec)}$

$K_m = 2.1 \text{ (lb/A)}$  the dc motor gain

$K_a = 1.3 \text{ (mA/g)}$  the dc gain of the accelerometer

$\zeta_a = 0.3 \text{ to } 0.8$  specified range of damping ratio of accelerometer

$\omega_a = 2\pi 500 \text{ (r/s)}$  specified minimum natural frequency of the accelerometer

$K_F = 30 \text{ (V/A)}$  dc gain on accelerometer preamp

$\tau_3 = 0.9 \text{ (msec)}$

$M_p = 1.65 \text{ (lbm)}$  mass of the moving mass

$M_B = 3.85 \text{ (lbm)}$  mass of base and non-moving (orthogonal) proof mass

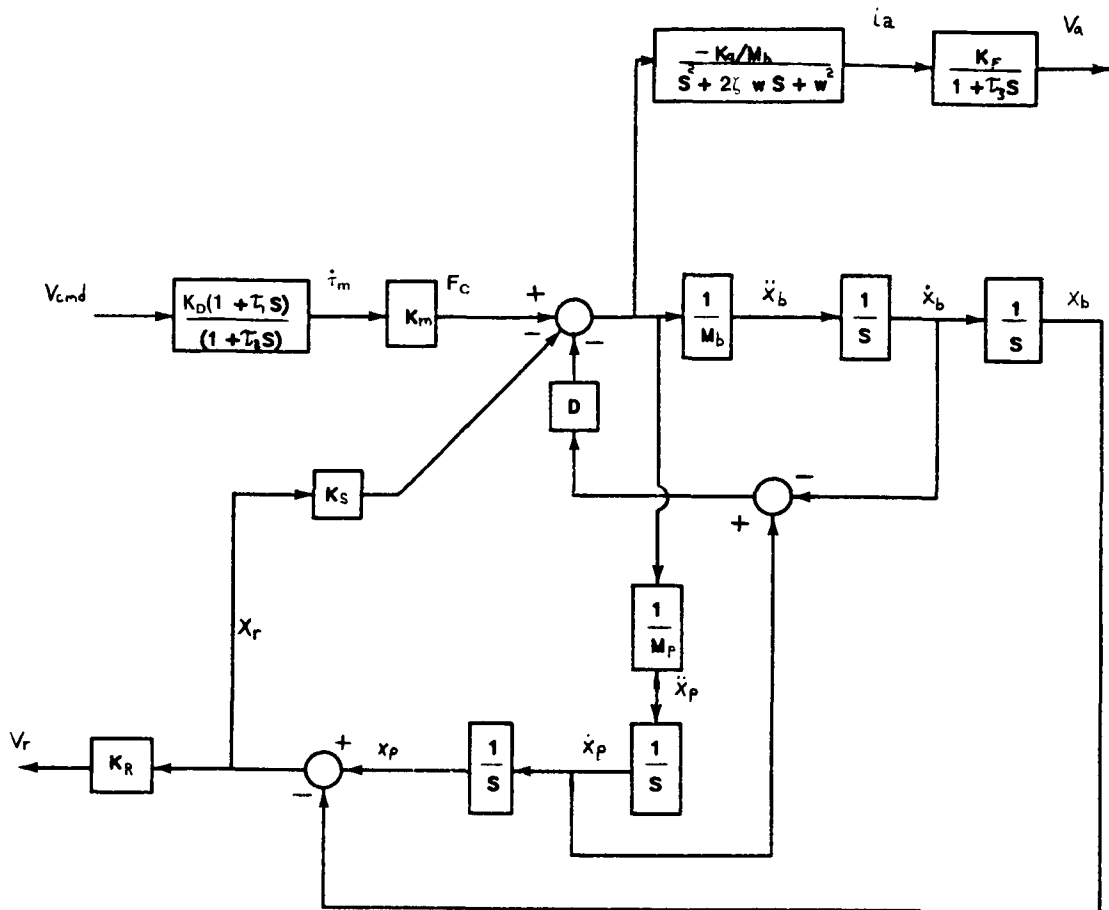


Figure 9. Block diagram of LMED analytical model.

$D = 0.046$  (lbf-s/in.) estimated damping coefficient

$K_s = 0.2$  (lbf/in.) the combined linear centering spring coefficient

$K_R = 20$  (V/in.) the LVDT gain

$V_{cmd} = \pm 10$  (V) the range of input command voltages

$i_m$  = (A) current into motor coil

$F_c$  = (lb) force produced by motor coil

$i_a$  = (A) output current from accelerometer

$V_a$  =  $\pm 10$  (V) range of accelerometer preamp return signal

$V_R$  =  $\pm 10$  (V) range of output voltage from LVDT

$X_p$  = (in.) motion of the proof mass in laboratory frame

$X_B$  = (in.) motion of the base in laboratory frame

$X_R$  = (in.) motion of proof mass relative to base .

Notice the motor dynamics do not include the effects of back emf produced by the velocity of the proof-mass permanent magnets relative to the motor coils. This effect is negligible due to the constant current feedback amplifier which drives the motor. Also note that the mass of the base includes the proof mass of the actuator mounted perpendicular to the modeled device.

There are no dynamics associated with the LVDT in the model since it was not used in the control loop. The LVDT data sheet specifies a 200 Hz cutoff frequency with less than 0.25 mV of ripple and 0.25 percent linearity.

The drive electronics transfer function was obtained from the schematic shown in Figure 10. Assuming an ideal operational amplifier (infinite gain high input impedance and low output impedance) the following transfer function between the common voltage and motor current can be obtained.

$$\frac{I_m}{V_{cmd}} = \frac{-A_o (R_L + Z_F) - R_L}{A_o R_L R_I + [(Z_m + \gamma) (R_I + R_L + Z_F) + R_L (R_I + Z_F)]}$$

where  $A_o$  = ideal amplifier gain  $> 10^6$

$$Z_F = \frac{R_F}{1 + C_F R_F s}$$

$$Z_m = \frac{(R_{M1} + 1/C_M s) (R_{M2} + L_M s)}{(R_{M1} + R_{M2}) + L_M s + 1/C_1 s}$$

$$\gamma = K_B K_M s \frac{M_B - M_P}{M_P M_B s^2 + (M_P + M_B) Ds + (M_P + M_B) K_s}$$

$$K_B = 0.237 \text{V/in./sec back emf constant} .$$

The transfer function  $I_m/V_{cmd}$  represents a constant current amplifier. Since  $A_o$  is large, this relation can be closely described by the approximation

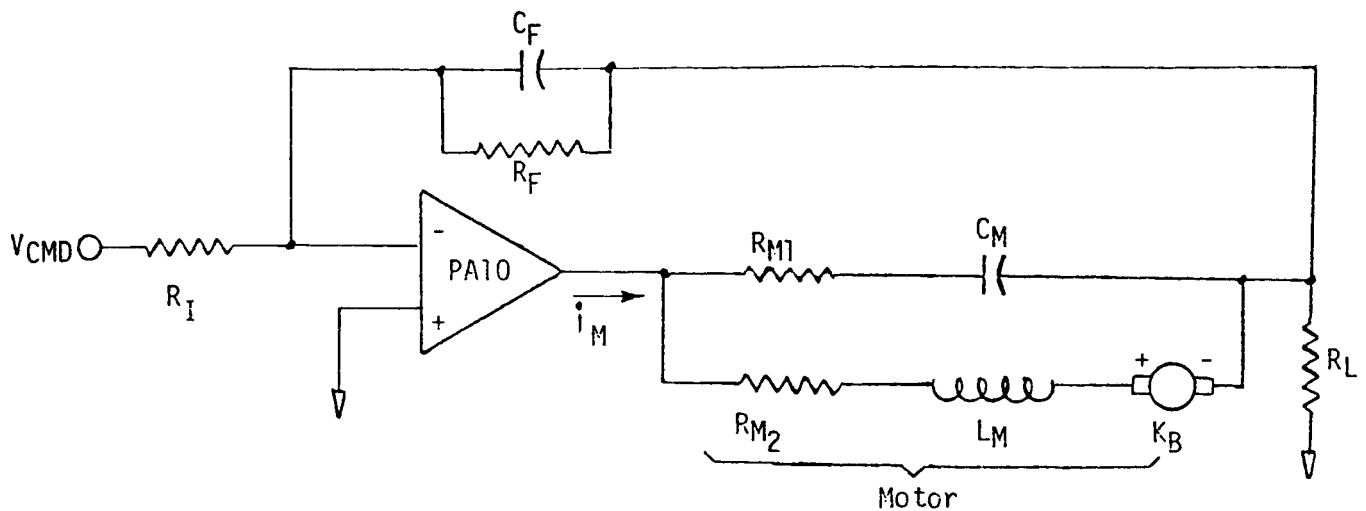
$$\frac{I_m}{V_{cmd}} = \frac{-R_L + Z_F}{R_L R_I} = \frac{-K_D (1 + \tau_1 s)}{1 + \tau_2 s}$$

The maximum error in this approximation is 2 percent which occurs at the 40 kHz resonance of  $Z_m$ . The term  $\gamma$  is highly damped so it has little influence compared to  $A_o$ . It does, however, encompass the back emf effect which shows that back emf need not be included when using a constant current source with high gain and high input impedance. Furthermore, since  $\tau_2 = 4 \times 10^{-5}$  sec, the drive electronics can be sufficiently represented by  $K_D$  at the structural frequencies, and the conversion from command volts to force becomes  $K_D K_m = 0.42$  (lbf/V).

The accelerometer preamplifier circuit is shown in Figure 11. The ideal operational amplifier assumption yields the transfer function

$$\frac{V_a}{i_a} = \frac{-R_1}{R_o} \frac{1}{1 + \tau_3 s}$$

where  $\tau_3 = C_1 R_1 = 0.9$  msec. The 177 Hz break frequency of the amplifier contributes only eight degrees of phase lag at 25 Hz, and may sometimes be neglected. Similarly, the 500 Hz low pass effects of the accelerometer may be neglected in some cases.



$R_I = 200\text{k}\Omega$	$R_F = 40\text{K}\Omega$	$R_{M1} = 1\Omega$	$C_M = 0.01\mu\text{f}$	$R_L = 1\Omega$
$C_F = 0.001\mu\text{f}$	$R_{M2} = 6\Omega$	$L_M = 1.52\text{mh}$		
$K_B = 0.237\text{v/in/sec}$				

Figure 10. Schematic of LMED drive electronics.

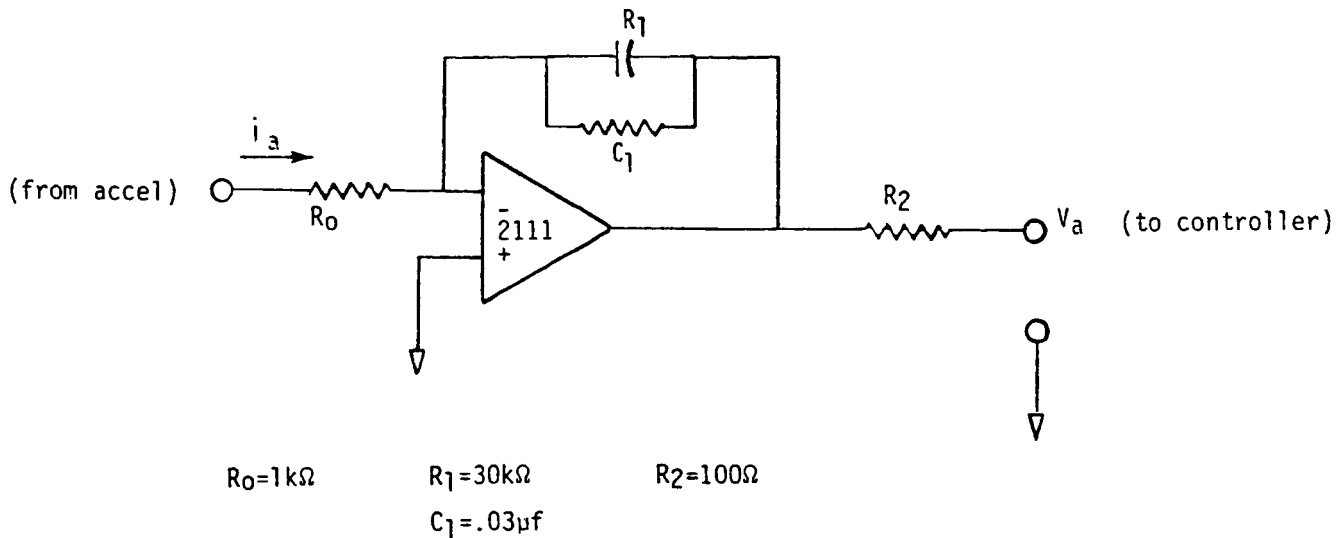


Figure 11. Accelerometer output amplifier schematic.

Figure 12b provides measured frequency response data for LMED C, taken in the laboratory. The LVDT response was obtained with the LMED base clamped to the laboratory test bench. The accelerometer response was obtained with the LMED floating on an air bearing. Figure 12a shows the predicted response using the ideal analytical models. The LVDT response compares well with measured data; the accelerometer response does not match measured data very well. A subsequent report from Control Dynamics to MSFC, entitled "Characterization and Hardware Modifications of LMEDs," describes the unmodeled nonlinearities of the LMEDs and the steps taken to linearize them. The hysteresis and stiction initially inherent to the LMEDs lead to the discrepancies seen.

### III. CONTROLLER DESIGNS

#### 3.1 MSFC Digital LMED Controller

To gain familiarity with the performance capabilities of the LMEDs, MSFC adopted a conservative control methodology. Since the vibration modes in Experiment 1 were clearly separable in frequency, a narrow bandwidth, digital, rate feedback controller was designed for each LMED. The center frequency of each controller was placed near the frequency of the dominant mode at that actuator location. Referencing back to Table 2, LMED A was tuned to the 1.96 Hz mode; LMED B to 2.78 Hz, LMED C to 11.8 Hz and LMED D to 12.88 Hz. Figure 13 provides the basic block diagram of the control algorithm. The HP-9000/COSMEC control computer samples the accelerometer pre-amplifier signals at a 50 Hz rate; the A/D input filters on the COSMEC were bypassed. The second-order digital filter performs both discrete time integration and bandpass filtering of the accelerometer signal. The narrow bandpass filter helps

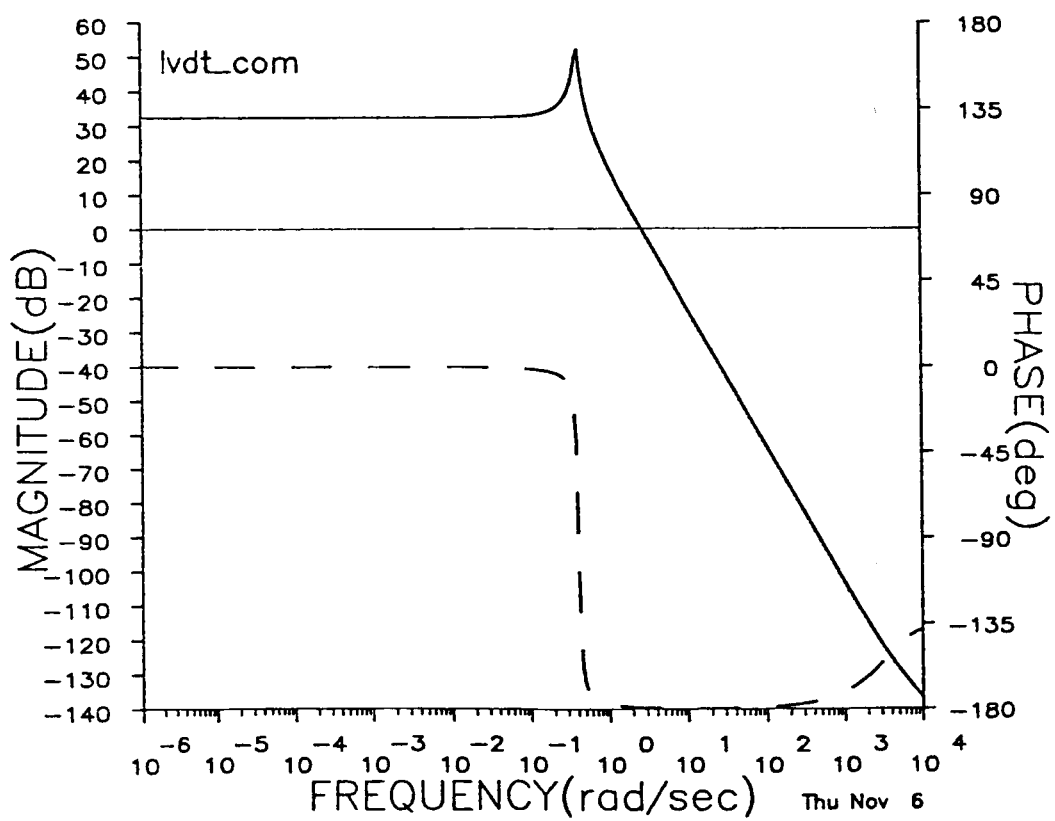
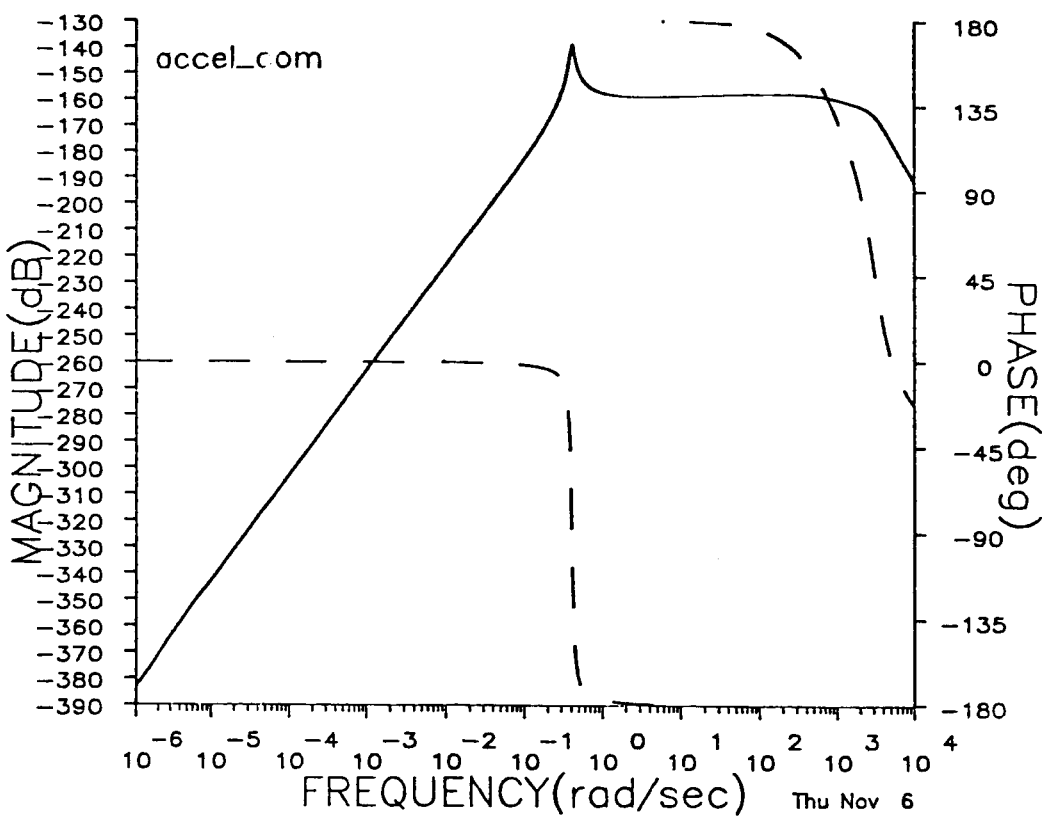


Figure 12a. Analytic frequency response from LMED to accelerometer.

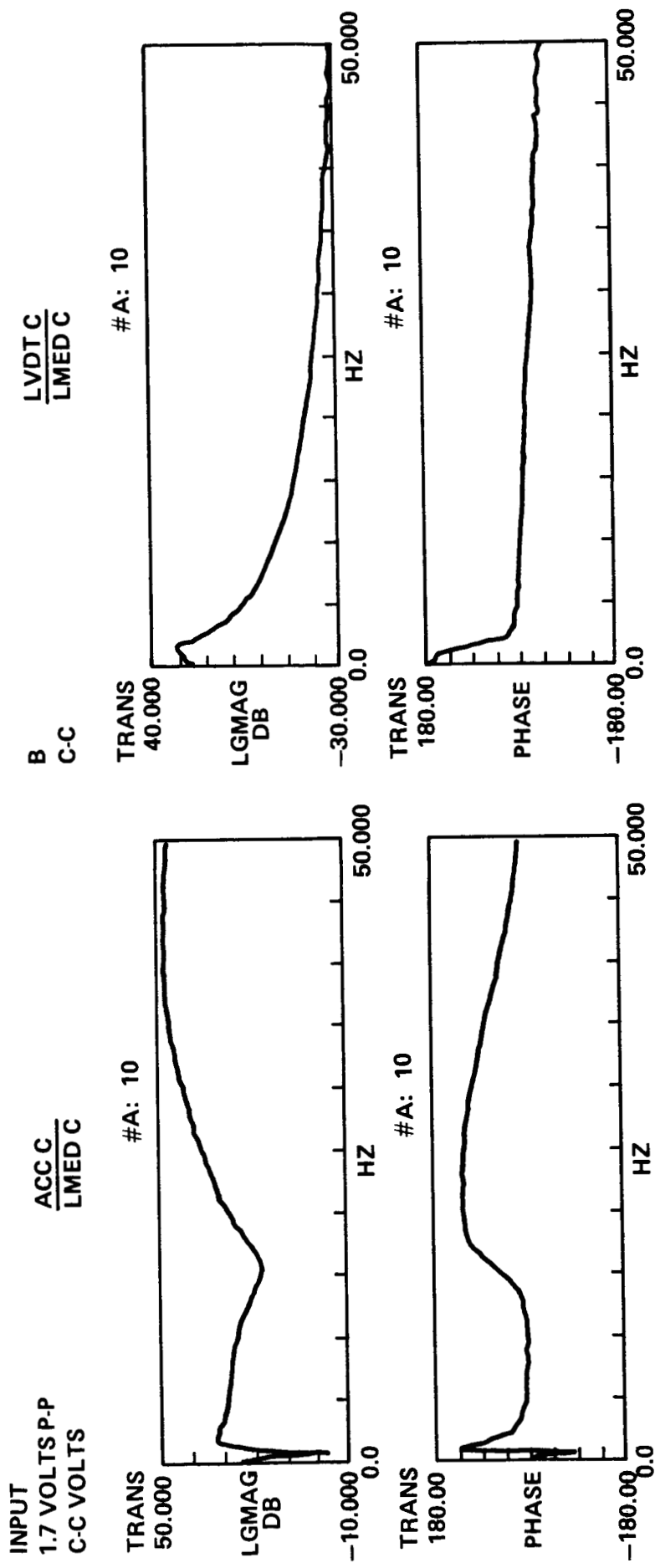


Figure 12b. Measured frequency response from LMED ( $V_{CMD}$ ) to accelerometer ( $V_A$ ) and LVDT ( $V_R$ ).

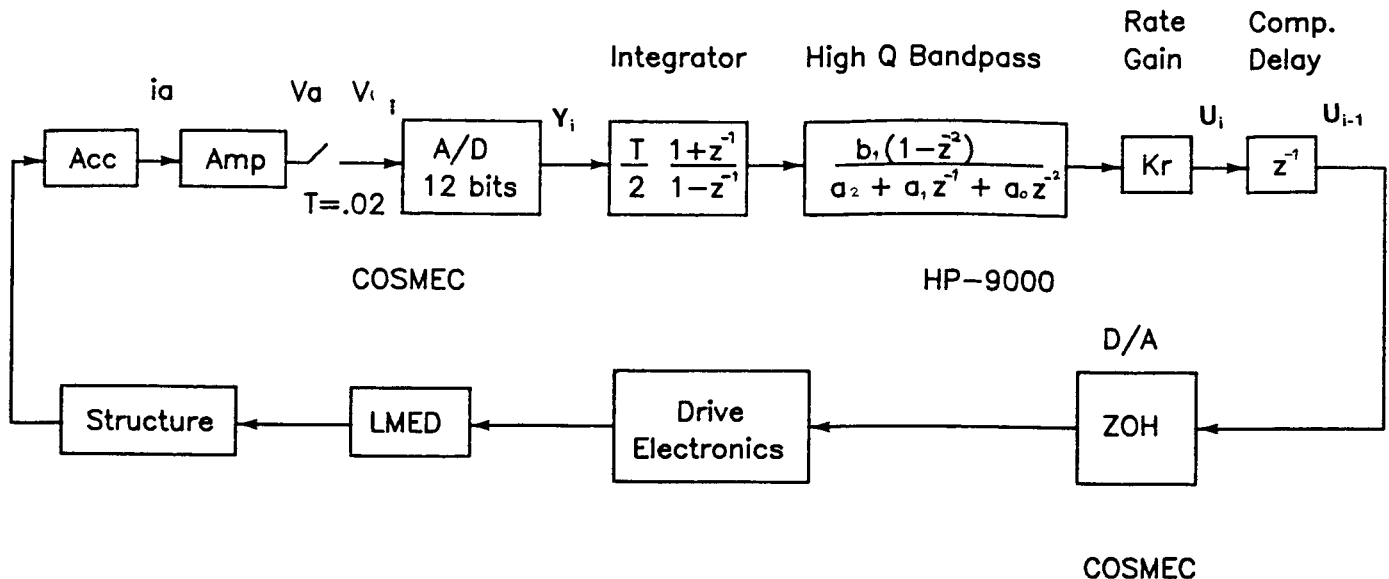


Figure 13. Block diagram of LMED digital controller.

reduce the effects of the LMED non-linearities. Note that in Figure 13 a unit delay  $z^{-1}$  accounts for a fixed computational delay of one sample period.

The filter coefficients are determined as follows. A second-order Butterworth bandpass filter is described by

$$G_{BP}(s) = \frac{(\omega_0/Q)s}{s^2 + (\omega_0/Q)s + \omega_0^2} = \frac{(\omega_2 - \omega_1)s}{s^2 + (\omega_2 - \omega_1)s + \omega_1\omega_2}$$

where

$$\omega_0 = 2\pi f_0 = \text{center frequency}$$

$$Q = \omega_0/\Delta\omega \quad \omega_1 = \omega_0^2/\omega_2$$

$$\Delta\omega = \omega_2 - \omega_1 = 3\text{db bandwidth} \quad \omega_2 = \omega_0 (1 + \sqrt{1 + 4Q^2})/(2Q)$$

This continuous filter is transformed to discrete time using the Tustin transformation with frequency prewarping;

$$s = \frac{2}{T} \frac{z-1}{z+1}$$

$$\Omega_1 = \frac{2}{T} \tan(\frac{1}{2} \omega_1 T)$$

$$\Omega_2 = \frac{2}{T} \tan(\frac{1}{2} \omega_2 T)$$

where  $T$  is the sample period. Substituting for  $s$  and replacing  $\Omega_1$ ,  $\Omega_2$  for  $\omega_1$ ,  $\omega_2$  results in

$$G_{BP}(z) = \frac{b_1(z^2-1)}{a_2 z^2 + a_1 z + a_0}$$

where

$$b_1 = (\gamma_2 - \gamma_1)$$

$$a_2 = 1 + \gamma_2 - \gamma_1 + \gamma_1 \gamma_2$$

$$a_1 = 2(\gamma_1 \gamma_2 - 1)$$

$$a_0 = 1 + \gamma_1 - \gamma_2 + \gamma_1 \gamma_2$$

$$\gamma_1 = \tan(\frac{1}{2}\omega_1 T) = \frac{1}{2}\Omega_1 T$$

$$\gamma_2 = \tan(\frac{1}{2}\omega_2 T) = \frac{1}{2}\Omega_2 T$$

The discrete time integration is accomplished by replacing 1/s with

$$\frac{T}{2} \frac{z+1}{z-1}$$

To implement the integrator filter with the control computer, the following reduction was made.

$$\frac{U(z)}{Y(z)} = \frac{T}{2} \frac{z+1}{z-1} \frac{b_1(z-1)(z+1)}{a_2 z^2 + a_1 z + a_0} = \frac{b_2 + b_1 z^{-1} + b_0 z^{-2}}{a_2 + a_1 z^{-1} + a_0 z^{-2}} , \quad b_0 = b_2 = \frac{1}{2} b_1$$

Taking the inverse Z transformation yields the discrete time algorithm

$$u_i = K_r (b_2 Y_i + b_1 Y_{i-1} + b_0 Y_{i-2} - a_1 u_{i-1} - a_0 u_{i-2}) / a_2$$

where  $K_r$  represents the desired rate feedback gain constant. The control algorithm was programmed so that  $K_r$ ,  $\omega_0$  and Q for each LMED could be specified at runtime. The following values were eventually used during experiment 1B.

	$f_o$	Q	$K_r$
LMED-A	5	10	-750
LMED-B	5	10	-600
LMED-C	12.5	10	-750
LMED-D	12.5	10	-600

### 3.2 MSFC Digital LMED/AGS Controller

In Experiment 2 the LMEDs were operated in parallel, i.e., simultaneously with the AGS torque motors. Because this experiment configuration closely resembled a previous MSFC experimental setup, a previously developed, low bandwidth AGS controller was modified to work with the LMEDs [1]. Although the resulting control law was functionally decentralized, the individual controllers were cast into state variable form to facilitate future analysis and investigation of other control methods. This particular control experiment was designed to demonstrate the functioning hardware and simple control techniques. The control gains and frequencies were selected largely experimentally to achieve a working closed loop system using seven control effectors and seven control sensors. The performance which was obtained was not fully supported analytically due mostly to the inherent non-linearities of the LMEDs which complicate such analyses. The following controller formulation, then is provided for future control studies involving more linear actuators. A description is also provided of how the control gains and frequencies were selected experimentally.

The discrete time filter given in the previous section can be expressed in the following state variable form

$$\begin{bmatrix} X_{c1} \\ X_{c2} \end{bmatrix}_{i+1} = \begin{bmatrix} 0 & -\alpha_2 \\ 1 & -\alpha_1 \end{bmatrix} \begin{bmatrix} X_{c1} \\ X_{c2} \end{bmatrix}_i + \begin{bmatrix} \beta_1 \\ \beta_2 \end{bmatrix} X_{s_i}$$

where

$$\alpha_2 = a_o/a_2$$

$$\beta_1 = (b_o - a_o b_2)/a_2$$

$$\alpha_1 = a_1/a_2$$

$$\beta_2 = (b_1 - a_1 b_2)/a_2$$

and  $Y_{ci} = K_r [X_{c2i} + (b_2/a_2) Y_i]$  where  $X_{si}$  represents the accelerometer preamplifier signal, and  $Y_{ci}$  is the control law output.

The structure, sensor, actuator and controller can be represented in the following state variable form:

structure	$\dot{X}_p = A_p X_p + B_p U_p$	$X_p = (2n_p \times 1)$ plant state vector
measurement	$Y_p = C_p X_p + D_p U_p$	$Y_p = (m \times 1)$ plant output vector
sensors	$\dot{X}_s = A_s X_s + B_s Y_p$	$X_s = (n_s \times 1)$ sensor state vector
actuators	$\dot{U}_p = A_u U_p + B_u Y_c$	$U_p = (n_u \times 1)$ plant input vector
control gains	$Y_{c_i} = C_c X_{c_i} + D_c X_{s_i}$	$Y_{c_i} = (\ell \times 1)$ controller output vector
control filter	$X_{c_{i+1}} = A_c X_{c_i} + B_c X_{s_i}$	$X_{c_i} = (n_c \times 1)$ controller state vector

Note that the control law is written in discrete time coordinates, where  $X_{s_i}$  is the  $i$ th sample of sensors  $X_s$ .  $X_{c_i}$  is the controller state at the  $i$ th sample and  $Y_{c_i}$  is the controller output determined at the  $i$ th sample. The relationships between these state equations are shown in Figure 14. The plant equations are most easily described in modal coordinates, in which  $n_p$  represents the number of vibration modes in the plant model;

$$X_p^T = [n_1 \ n_2 \ \dots \ n_{n_p} \ n_{n_p}]$$

where  $n_i$  represents the  $i$ th mode;  $A_p$  is block diagonal with each modal block  $A_{p_i}$  given by

$$A_{p_i} = \begin{bmatrix} 0 & 1 \\ -\omega_i^2 & -2\zeta_i \omega_i \end{bmatrix}$$

where  $\omega_i$  and  $\zeta_i$  are the  $i$ th modal frequency and damping; and  $B_p$  is given by

$$B_p^T = \begin{bmatrix} 0 & b_{11} & 0 & b_{12} & \dots & 0 & b_{1n_p} \\ 0 & b_{21} & 0 & b_{22} & \dots & 0 & b_{2n_p} \\ \vdots & | & | & | & \ddots & | & \vdots \\ \vdots & | & | & | & \ddots & | & \vdots \\ 0 & b_{\ell 1} & 0 & b_{\ell 2} & \dots & 0 & b_{\ell n_p} \end{bmatrix}$$

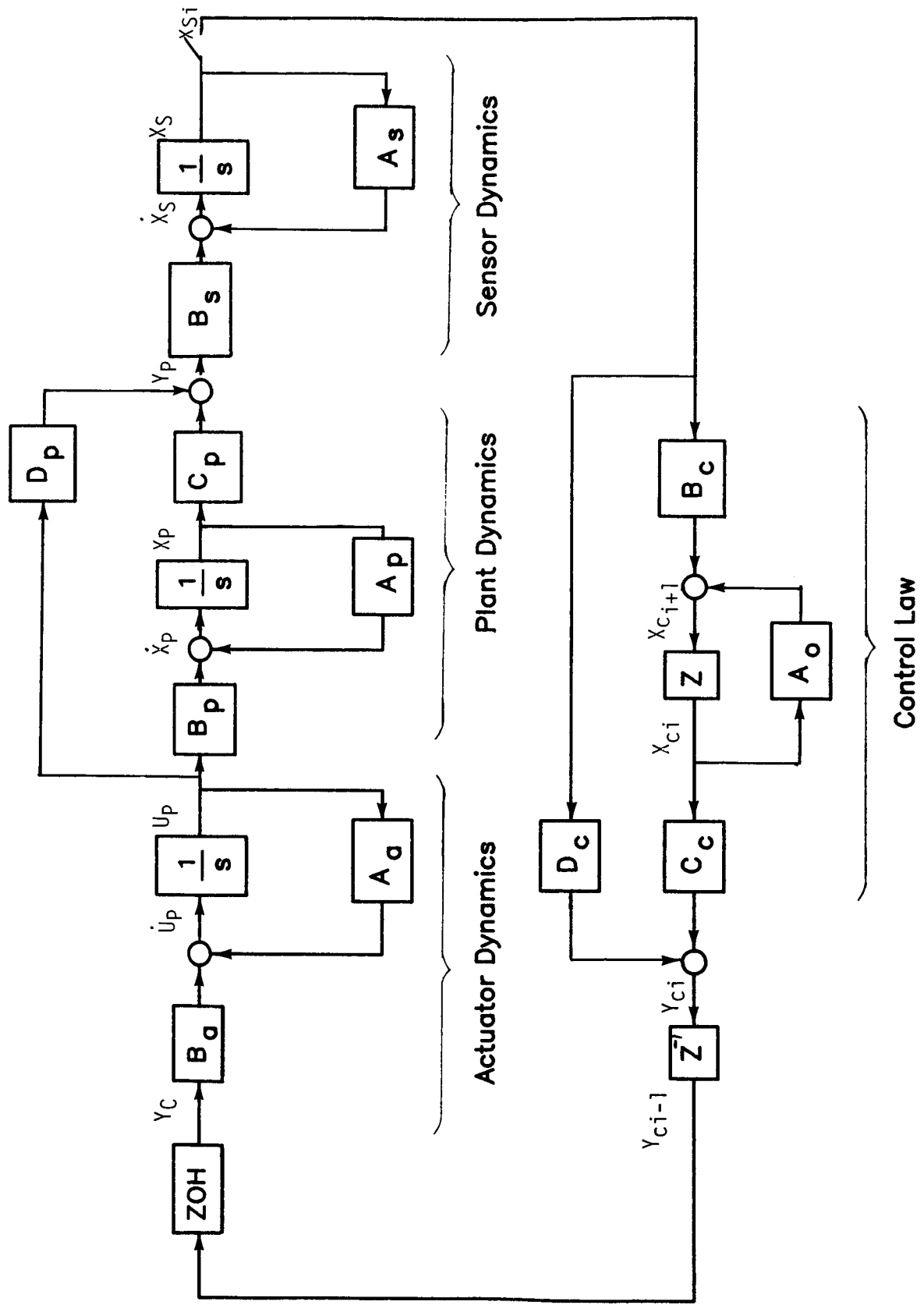


Figure 14. State space model of digital AGS/LMED controller and plant.

where  $b_{ij}$  = jth mode shape at the ith actuator. The matrices  $C_p$  and  $D_p$  are obtained as follows: Let  $Y_p = C_1 X_p + C_2 \dot{X}_p$ , where  $C_1$  and  $C_2$  each resemble  $B^T p$ . In particular, for each mode  $j$ ,  $j = 1, 2, \dots, n_p$ , each  $(2j-1)$  column of  $C_1$  contains mode shapes at each proportional measurement, each  $(2j)$  column of  $C_1$  contains mode shapes at each rate sensor, and each  $(2j)$  column of  $C_2$  contains mode shapes for each acceleration measurement; otherwise, the elements of  $C_1$  and  $C_2$  are zero. Substituting  $\dot{X}_p = A_p X_p + B_p U_p$  into the above description for  $Y_p$  gives  $Y_p = C_p X_p + D_p U_p$  where  $C_p = (C_1 + C_2 A_p)$  and  $D_p = C_2 B_p$ . Taking advantage of the inertial reference data provided by the HP-9000,  $C_1$  provides angular position information from the base gyros while  $C_2$  provides the accelerometer information from each LMED. The sensor dynamics provide first order approximations for the gyro (40 Hz bandwidth) and accelerometer (50 Hz) electronics. Therefore,  $n_s = m$ , and both  $A_s$  and  $B_s$  are ( $m \times m$ ) diagonal matrices, with the negative of the sensor break frequencies (radians/second) along  $A_s$  and the sensor gain (volts/physical units) along  $B_s$ . The actuator dynamics need only represent the first order models of the AGS torque motors which have 100 Hz bandwidths. The LMED bandwidths exceed 2 KHz, which implies  $n_u = l$ . For some analyses even the AGS dynamics can be neglected since the phase lag is less than 12 degrees at 20 Hz. The discrete time control law is also block diagonal, with each block resembling the  $(2 \times 2)$  control law given at the beginning of this section; this implies that  $n_c = 2m$ .

For control law design and analysis it is convenient to discretize the continuous time equations. To do this, consider the following augmented state equation

$$\begin{bmatrix} \dot{X}_p \\ \dot{X}_s \\ \dot{U}_p \end{bmatrix} = \begin{bmatrix} A_p & 0 & B_p \\ B_s C_p & A_s & B_s D_p \\ 0 & 0 & A_u \end{bmatrix} \begin{bmatrix} X_p \\ X_s \\ U_p \end{bmatrix} + \begin{bmatrix} 0 \\ 0 \\ B_u \end{bmatrix} [Y_c]$$

which can be written  $\dot{X} = AX + BU$ . The system can be discretized for a sample period  $T$ , taking into account the constant computational delay of one sample period. The resulting system is given by

$$X_{i+1} = \hat{A}X_i + \hat{B}U_{i-1}$$

where

and

$$\hat{B} = \int_0^T e^{At} dt B .$$

Defining additional states  $V_i = U_{i-1}$ , this can be expressed as

$$\begin{bmatrix} X_{i+1} \\ V_{i+1} \end{bmatrix} = \begin{bmatrix} A & B \\ 0 & 0 \end{bmatrix} \begin{bmatrix} X_i \\ V_i \end{bmatrix} + \begin{bmatrix} 0 \\ I_{n_u} \end{bmatrix} U_i .$$

The discrete time measurement equation becomes

$$[X_{s_i}] = [\zeta \ 0] \begin{bmatrix} X_i \\ V_i \end{bmatrix}$$

where  $\zeta = [0_{2n_p} \ I_{ns} \ 0_{nu}]$ ,  $I_{ns}$  = identity matrix, and  $0_{2n_p}$ ,  $0_{nu}$  are zero matrices. Combining the control filter equations with the above gives

$$\begin{bmatrix} X_{i+1} \\ V_{i+1} \\ X_{ci+1} \end{bmatrix} = \begin{bmatrix} A & B & 0 \\ 0 & 0 & 0 \\ B_c \zeta & 0 & A_c \end{bmatrix} \begin{bmatrix} X_i \\ V_i \\ X_{ci} \end{bmatrix} + \begin{bmatrix} 0 \\ I_{nu} \\ 0 \end{bmatrix} U_i$$

or  $X_{i+1} = A X_i + B U_i$

$$Y_i = CX_i \quad \text{where} \quad C = \begin{bmatrix} \zeta & 0 & 0 \\ 0 & 0 & I_{nc} \end{bmatrix}$$

$$U_i = KY_i \quad \text{where} \quad K = [D_c \ C_c] .$$

This places the entire system in standard discrete time, state variable form. The elements of the gain  $K$  and the filter element  $A_c$  and  $B_c$  can be modified at the

control designer's option. In Experiment II, these elements were determined by examination of measured open loop frequency response data. The open loop transfer function from each actuator to its associated sensor determines the relative level of control authority over each mode. Experiment I had shown poor LMED performance, especially with respect to low frequency modes. Thus, the AGS torquers were tuned to provide proportional-plus-derivative control of the cluster of modes near 1 Hz. The middle LMEDs (A and B) provide rate feedback control of the 4.5 Hz modes, and the lower LMEDs were tuned to the 8 Hz modes. The following control filter and gain matrices were obtained. The experimental results are discussed in the following section.

$$\begin{aligned} \mathbf{x}_s^T &= [\theta_x \theta_y \theta_z \ddot{x}_A \ddot{x}_B \ddot{x}_C \ddot{x}_D] \\ &\quad \text{base rate LMED accelerations} \\ &\quad \text{gyros} \\ \mathbf{A}_c &= \text{diagonal } [A_{cx} A_{cy} A_{cz} A_{ca} A_{cb} A_{cc} A_{cd}] \\ &\quad (14 \times 14) \end{aligned}$$

where

$$\begin{aligned} A_{cx} = A_{cy} = A_{cz} &\triangleq E = \begin{bmatrix} .1270 & .001873 \\ -29.545 & -.2026 \end{bmatrix} \\ A_{ca} &= \begin{bmatrix} 0 & -\alpha_{2A} \\ 1 & -\alpha_{1A} \end{bmatrix} \quad \alpha_{1A} = -1.49245 \quad \alpha_{2A} = 0.75575 \\ A_{cb} &= \begin{bmatrix} 0 & -\alpha_{2B} \\ 1 & -\alpha_{1B} \end{bmatrix} \quad \alpha_{1c} = -1.39408 \quad \alpha_{2B} = 0.72654 \\ A_{cc} &= \begin{bmatrix} 0 & -\alpha_{2C} \\ 1 & -\alpha_{1C} \end{bmatrix} \quad \alpha_{1c} = -0.72373 \quad \alpha_{2c} = 0.71971 \\ A_{cd} &= \begin{bmatrix} 0 & -\alpha_{2D} \\ 1 & -\alpha_{1D} \end{bmatrix} \quad \alpha_{1d} = -0.51073 \quad \alpha_{2d} = 0.6928 \end{aligned}$$

$$\begin{aligned} \mathbf{B}_c &= \text{diagonal } [B_{cx} B_{cy} B_{cz} B_{cA} B_{cB} B_{cC} B_{cD}] \\ &\quad (14 \times 7) \end{aligned}$$

where

$$B_{cx} = B_{cy} = B_{cz} \triangleq F = \begin{bmatrix} 5.534E-5 \\ 1.8728E-3 \end{bmatrix}$$

$$B_{cA} = \begin{bmatrix} \beta_{1A} \\ \beta_{2A} \end{bmatrix} = \begin{bmatrix} 8.468E-5 \\ 4.687E-3 \end{bmatrix}$$

$$B_{cB} = \begin{bmatrix} \beta_{1B} \\ \beta_{2B} \end{bmatrix} = \begin{bmatrix} 9.3962E-5 \\ 5.178E-3 \end{bmatrix}$$

$$B_{cC} = \begin{bmatrix} \beta_{1C} \\ \beta_{2C} \end{bmatrix} = \begin{bmatrix} -2.4993E-5 \\ 4.4633E-3 \end{bmatrix}$$

$$B_{cD} = \begin{bmatrix} \beta_{1D} \\ \beta_{2D} \end{bmatrix} = \begin{bmatrix} -3.957E-4 \\ 4.496E-3 \end{bmatrix}$$

$$C_c = \text{diagonal } [C_{cx} \ C_{cy} \ C_{cz} \ C_{cA} \ C_{cB} \ C_{cC} \ C_{cD}]  
(7 \times 14)$$

where

$$C_{cx} = [K_{rx} \ G \ E] = [4.667E7 \quad 3.198E5]$$

$$C_{cy} = [K_{ry} \ G \ E] = [5.599E7 \quad 3.838E5]$$

$$C_{cz} = [K_{rz} \ G \ E] = [9.332E6 \quad 6.396E4]$$

$$C_{cA} = [0 \ K_{rA}] = [0 \quad -200]$$

$$C_{cB} = [0 \ K_{rB}] = [0 \quad -200]$$

$$C_{cC} = [0 \ K_{rC}] = [0 \quad -90]$$

$$C_{cD} = [0 \ K_{rD}] = [0 \quad -100]$$

$$D_c = \text{diagonal } [D_{cx} \ D_{cy} \ D_{cz} \ D_{cA} \ D_{cB} \ D_{cC} \ D_{cD}]$$

$$= \text{diagonal } [(K_{px} + K_{rx} GF) \ (K_{py} + K_{ry} GF) \ (K_{pz} + K_{rz} GF) \ (-\beta_{oA}) \ (-\beta_{oB}) \ (-\beta_{oC}) \ (-\beta_{oD})]$$

In the above definitions, matrices E, F, and G are those derived for a previous GF/LSSCV experiment;  $G = [1.58E4 \ 1.58E5]$  while E and F are defined for matrices  $A_c$  and  $B_c$ . The gains  $K_{ri}$  represent rate feedback gains for the ith channel, and  $K_{pi}$  is the corresponding position gain; the following values were used:  $K_{px} = 1000$ ,  $K_{py} = 1200$ ,  $K_{pz} = 200$ , and  $K_{rx} = -10$ ,  $K_{ry} = -12$ ,  $K_{rz} = -2$ . The remaining parameters ( $\alpha_2$ ,  $\alpha_1$ ,  $\beta_o$ ,  $\beta_1$ ,  $\beta_2$ ,  $K_r$ ) for LMEDs A, B, C, and D were identified at the beginning of this section. Basic control equations are given in Table 4.

#### IV. EXPERIMENTAL RESULTS

This section presents selected portions of experimental results which are indicative of the performance obtained with the LMEDs. Results for each of the three controllers are presented separately. Section V contains some analysis and conclusions applicable to the data. The frequency response plots were obtained with an HP-5423 Dynamic Analyzer using bandlimited white noise for the input commands. Time history data was recorded with the HP-9000/COSMEC control computer and an analog strip-chart recorder.

##### 4.1 Experiment 1B: MSFC Digital Controller

Obtaining results during this experiment required more time than expected. Hardware problems in the control computer led to further delays. To interface the VCOSS hardware with the GF/LSSCV control computer, new software had to be written and verified, and the I/O capacity of the COSMEC had to be increased. These software changes were made along with a major reconfiguration of the main program, converting previously used assembly language segments from the COSMEC into HP-Basic. The additional I/O channels created intermittent problems with the current drive on one of the A/D converters. Meaningful data was nonetheless obtained as shown in Figure 15. The test configuration was with the AGS gimbals unlocked, and with the GF/LSSCV control computer active. Trial and error, with some simulation and analysis, led to the control gains and frequencies listed in Section 3.2. Again, very little performance was obtained from LMED-D. Figure 15a shows the open-loop response of each accelerometer to the excitation source at 4 Hz. Figure 15b shows performance gains with only LMED-A operating; notice the slight coupling into channel B. Figure 15c shows the analogous result with only LMED-B operating closed-loop. Finally, Figure 15d shows the effect of operating all four LMEDs. Since the lower devices (C and D) were tuned to 12.5 Hz, they contributed little to this case. LMED-C

TABLE 4. BASIC CONTROL EQUATIONS

Basic Control Equations

$$\text{Basic Equations: } \dot{\underline{x}}_p = \begin{matrix} A_p \\ (2np \times 1) \end{matrix} \begin{matrix} x_p \\ (2np \times 2np) \end{matrix} \begin{matrix} x_p \\ (2np \times 1) \end{matrix} + \begin{matrix} B_p \\ (2np \times \ell) \end{matrix} \begin{matrix} u_p \\ (\ell \times 1) \end{matrix}$$

$$\dot{\underline{x}}_s = \begin{matrix} A_s \\ (ns \times ns) \end{matrix} \begin{matrix} x_s \\ (ns \times 1) \end{matrix} + \begin{matrix} B_s \\ (ns \times m) \end{matrix} \begin{matrix} y_p \\ (m \times 1) \end{matrix}$$

$$\dot{\underline{u}}_p = \begin{matrix} A_u \\ (\ell \times \ell) \end{matrix} \begin{matrix} u_p \\ (\ell \times 1) \end{matrix} + \begin{matrix} B_u \\ (\ell \times \ell) \end{matrix} \begin{matrix} y_c \\ (\ell \times 1) \end{matrix}$$

$$\dot{y}_p = \begin{matrix} C_p \\ (m \times 2np) \end{matrix} \begin{matrix} x_p \\ (2np \times 1) \end{matrix} + \begin{matrix} D_p \\ (m \times \ell) \end{matrix} \begin{matrix} u_p \\ (\ell \times 1) \end{matrix}$$

$$\dot{x}_{c_i} = \begin{matrix} A_c \\ (nc \times nc) \end{matrix} \begin{matrix} x_{c_i} \\ (nc \times 1) \end{matrix} + \begin{matrix} B_c \\ (nc \times ns) \end{matrix} \begin{matrix} x_s \\ (ns \times 1) \end{matrix}$$

Discrete plant, sensor, actuators:

$$\dot{\underline{x}}_{i+1} = \begin{matrix} \hat{A} \\ (nd \times 1) \end{matrix} \begin{matrix} x_i \\ (nd \times 1) \end{matrix} + \begin{matrix} \hat{B} \\ (nd \times \ell) \end{matrix} \begin{matrix} u_i \\ (\ell \times 1) \end{matrix}$$

$$\text{where } nd = 2np + ns + \ell \quad \underline{x}_i^T = [x_{pi}^T \quad x_{si}^T \quad u_{pi}^T]_{\ell}$$

$$\dot{x}_{s_i} = \begin{matrix} \zeta \\ (ns \times nd) \end{matrix} \begin{matrix} x_i \\ (nd \times 1) \end{matrix} + \begin{matrix} 0 \\ (ns \times \ell) (\ell \times 1) \end{matrix} \begin{matrix} v_i \\ (\ell \times 1) \end{matrix}; \quad \zeta = [0 \quad I_{ns} \quad 0]_{2np}$$

Controller equations:

$$\dot{x}_{c_{i+1}} = \begin{matrix} A_c \\ (nc \times nc) \end{matrix} \begin{matrix} x_{c_i} \\ (nc \times 1) \end{matrix} + \begin{matrix} B_c \\ (nc \times ns) \end{matrix} \begin{matrix} x_{s_i} \\ (ns \times 1) \end{matrix} = \begin{matrix} A_c \quad x_c \\ (ns \times ns) \end{matrix} + \begin{matrix} B_c \quad \zeta \\ (ns \times ns) \end{matrix} \begin{matrix} x_i \\ (ns \times nd) \end{matrix}$$

$$\text{where } nc = 2ns = 2m$$

$$\dot{y}_{c_i} = \begin{matrix} C_c \\ (\ell \times nc) \end{matrix} \begin{matrix} x_{c_i} \\ (nc \times 1) \end{matrix} + \begin{matrix} D_c \\ (\ell \times ns) \end{matrix} \begin{matrix} x_{s_i} \\ (ns \times 1) \end{matrix}$$

Augmented state equations:

$$\dot{\bar{x}}_i = \begin{matrix} C \\ (ns + nc \times nd + \ell + nc) \end{matrix} \begin{matrix} x_i \\ (nd + \ell + nc \times 1) \end{matrix}$$

$$\dot{\bar{u}}_i = \begin{matrix} K \\ (\ell \times ns + nc) \end{matrix} \begin{matrix} \bar{x}_i \\ (ns + nc) \end{matrix}$$

$$\underline{x}_i^T = [(x_{pi}^T \quad x_{si}^T \quad u_{pi}^T)_{\ell} \quad v_i^T \quad x_{c_i}^T]_{nc} \quad \dot{\bar{x}}_i^T = [x_{s_i}^T \quad x_{c_i}^T]_{nc}$$

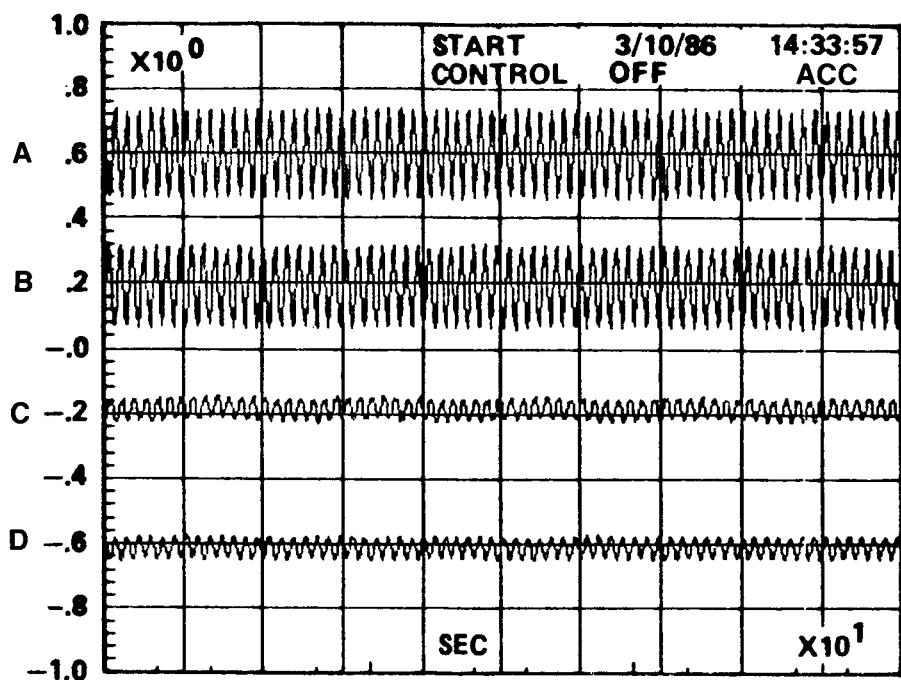


Figure 15a. Open loop response each acceleration to the BET at 5 Hz.

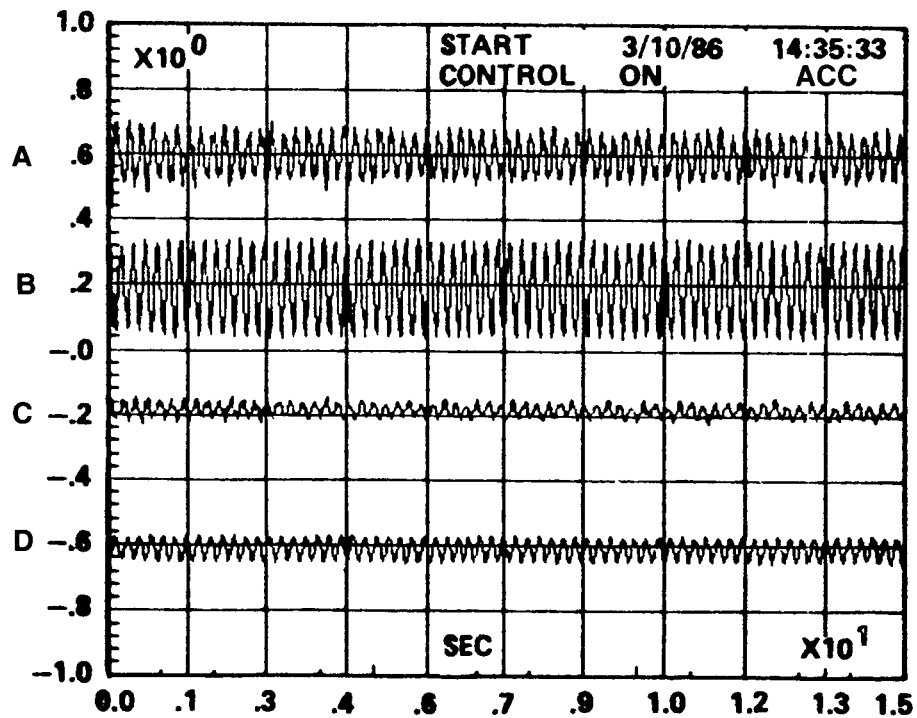


Figure 15b. Response with LMED-A only closed loop.

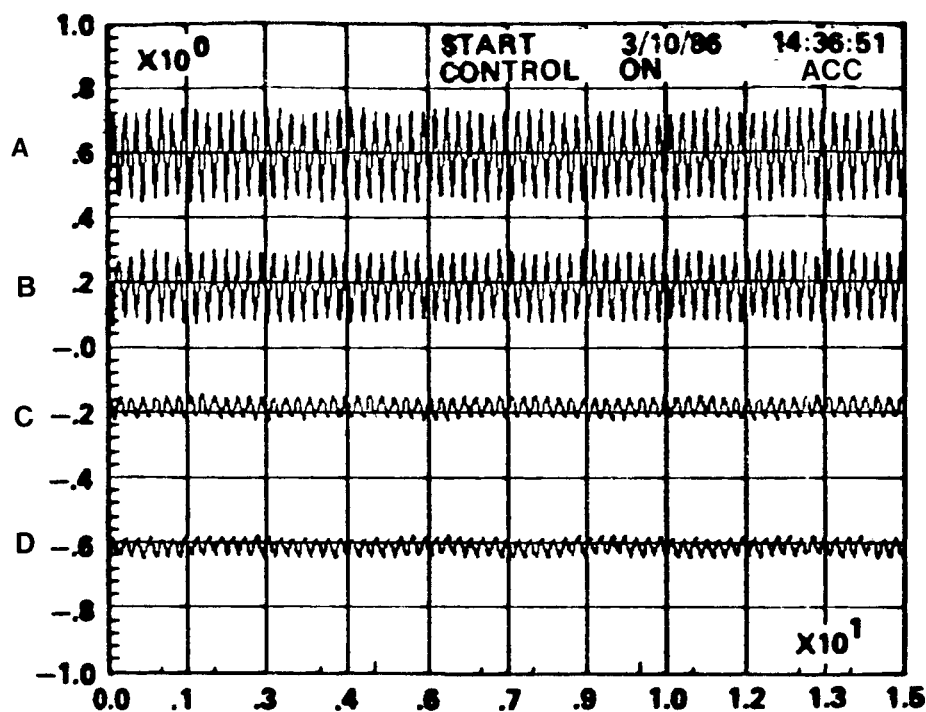


Figure 15c. Response with LMED-B only closed loop.

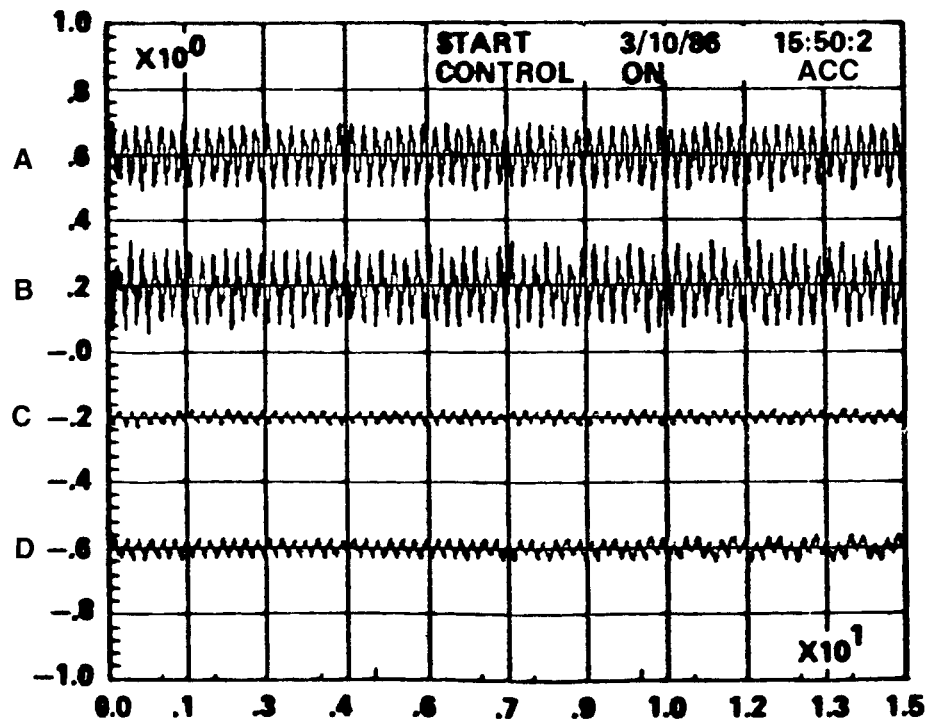


Figure 15d. Response with all LMEDs closed loop.

could effectively damp the 12.5 Hz mode, but in the process destabilized other modes. At this point, a linearity test was made using the LVDT on LMED-E (the device most visible from the control room). Figure 16 shows the open-loop response of LMED-E to low amplitude (0.1 V peak) triangular input signals at various frequencies below 1 Hz. Figure 17 shows the response to constant frequency (0.1 Hz) varying amplitude triangular commands. Non-linear behavior is most obvious. At this point, the experiment was discontinued so that the devices could be analyzed more closely on a laboratory bench. Results from the device characterization tests are documented in a separate report.

**OPEN LOOP RESPONSE OF LMED E: CONSTANT AMPLITUDE (0.1 VPEAK)  
VARYING FREQUENCY (0.1 TO 1.0 Hz)**

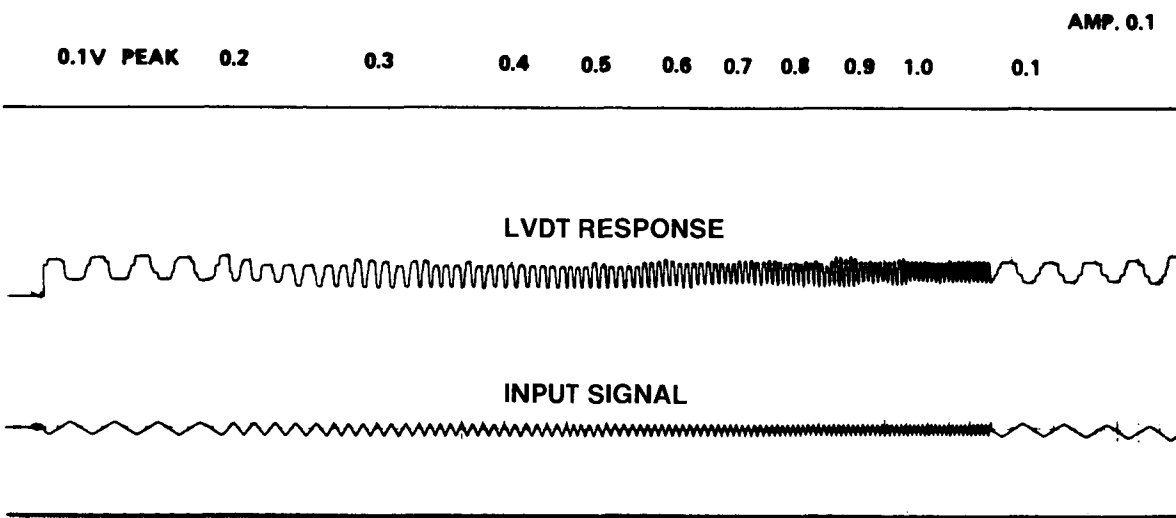


Figure 16. LMED-E linearity check: LVDT response to constant amplitude, varying frequency.

**OPEN LOOP RESPONSE OF LMED-E: CONSTANT FREQUENCY (0.1 Hz)  
VARY AMPLITUDE (0.1 to 1.0)**

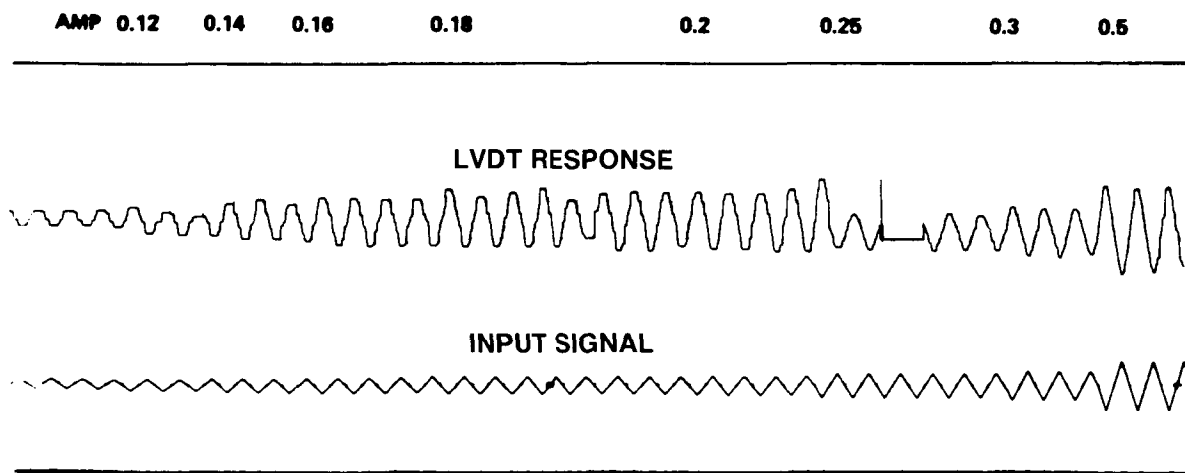


Figure 17. LMED-E linearity check: LVDT response to constant frequency, varying amplitudes.

#### 4.2 Experiment 2: MSFC 1 MED and AGS Controller

Experiment 1 determined that the LMEDs were not operating in a linear fashion. At that point, the lower pair of devices (C and D) were removed from the test article and examined on a laboratory bench. In addition to mechanical misalignments and bearing contamination, the devices exhibited significant hysteresis and bearing roughness. At the same time, program schedules for future GF/LSSCV experiments required that the VCOSS experiments come to a conclusion.

It was thus decided to use the spare LMED as an engineering model to reduce the dominant nonlinearities. The other LMEDs were used, as delivered, to demonstrate simultaneous operation of the AGS torquers and LMEDs in a decentralized control scheme. Schedule constraints permitted only a day and a half to develop and demonstrate this complement of control hardware. Thus, a largely cut and try approach was undertaken.

Figures 18 through 20 are sufficient to explain the procedure used. The control algorithms were predetermined as discussed in Section 3.3; only the control gains and frequencies need be determined. Figure 18 shows the open-loop frequency response between LMED-A and its accelerometer. Clearly, the mode at 4.4 Hz should be controlled by the actuator. The previous results, however, demonstrated that this control effort destabilized other modes. For example, Figure 19 shows the relationship between the y-axis torque motor and accelerometer A; the upper response was obtained with LMED-A in the open-loop condition and the lower response with LMED-A operating closed-loop. The 4.4 Hz mode is virtually eliminated, but the 1 Hz mode has been destabilized. Not shown here is the destabilizing effect on a nearby 8.5 Hz mode. The y-axis torque motor was thus commanded to squelch the low frequency modes (below 2 Hz). The upper trace in Figure 20 shows an expanded open-loop view of that of Figure 19. The lower response incorporates both LMED-A and y-axis torquer closed-loops. Comparing Figures 19 and 20 the lower frequency modes have been actively damped, but the 8.4 Hz mode has been destabilized. The open-loop response at LMED-C would suggest sufficient control at 8 Hz to reduce this response as before. However, the device non-linearities prevented success in that approach. Figure 21 shows the performance gains obtained by LMEDs A and B independently at their control frequencies. Figure 22 shows the AGS control effectiveness at 1 Hz with the LMEDs also operating; damping is effectively doubled by visual inspection. Figure 23 provides a dramatic demonstration of the effectiveness of LMED-B over a 5 Hz mode with all of the other actuators operating. (This response was obtained during a demonstration for the MSFC Workshop on Structural Dynamic and Control Interaction of Flexible Structures in April 1986.) Finally, the transient response of this control system is seen in Figure 24 by comparing open and closed loop responses to step commands on the Base Excitation Table.

#### V. CONCLUSIONS

- 1) The VCOSS-II LMEDs have the demonstrated capability to actively increase the damping of the LSS test article, using narrow band control filters. Experiment 1B shows 60 percent increase in the damping of the controlled modes. In Experiment 2 the LMED virtually eliminated the controlled vibration mode at 5 Hz.
- 2) Non-linearities of the LMEDs make broadband control applications difficult.

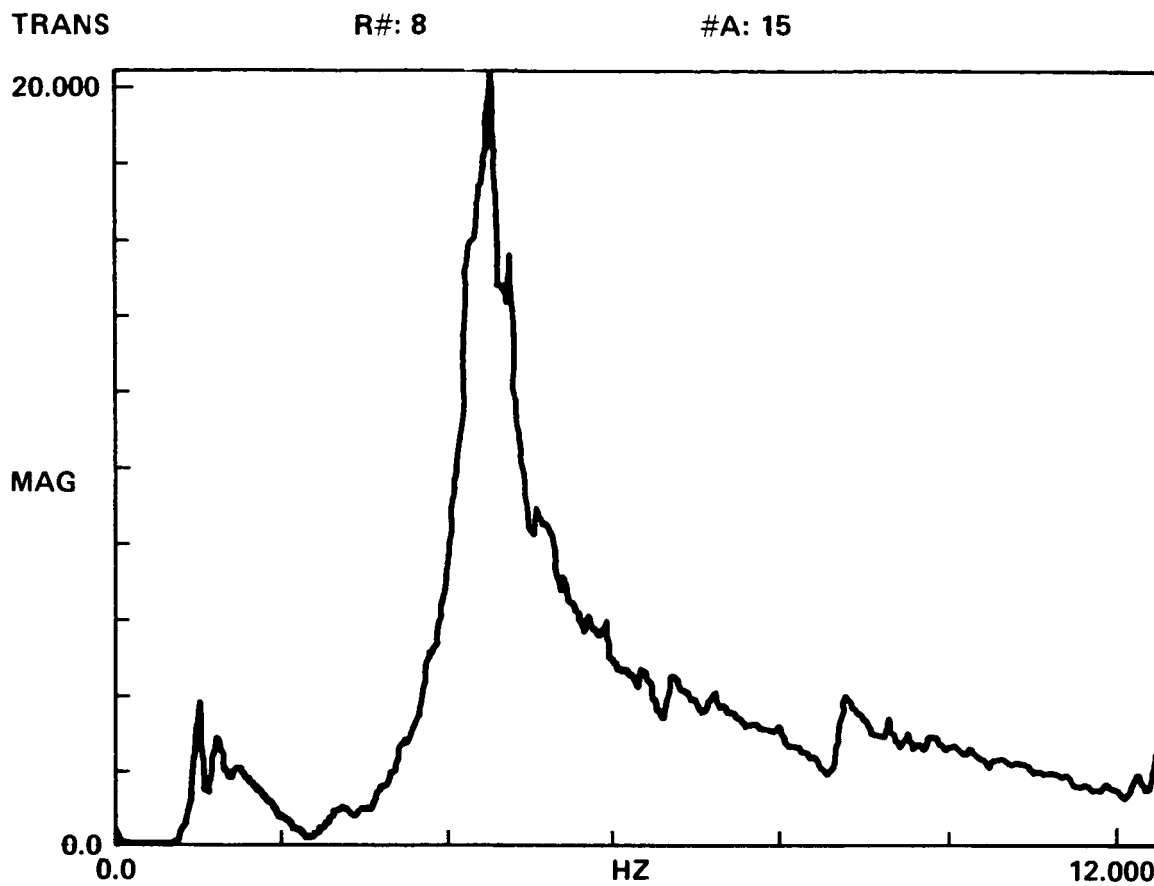


Figure 18. Magnitude of LMED-A to Acc-A transfer function in configuration 2; open loop.

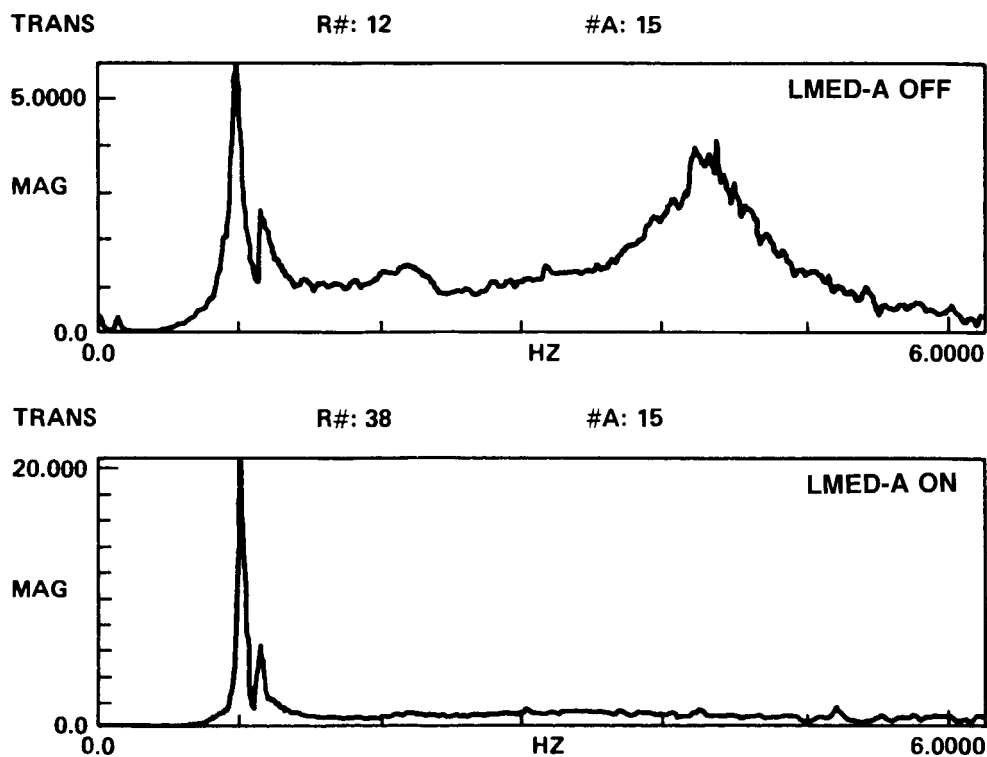


Figure 19. Magnitude of torque-Y to Acc-A transfer function in configuration 2; (open loop) LMEDA.

Closed loop effects of LMED-A on Y-torquer to Acc-A transfer function.

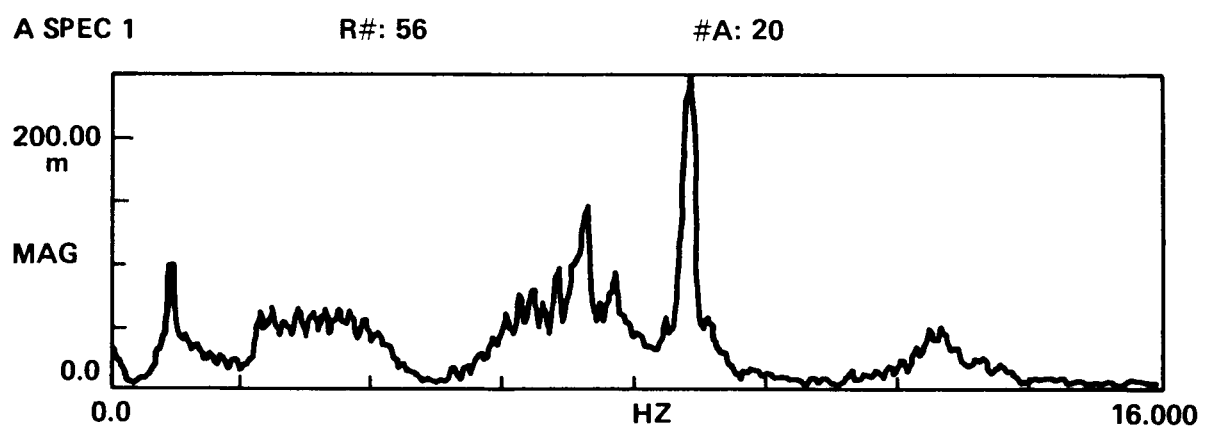
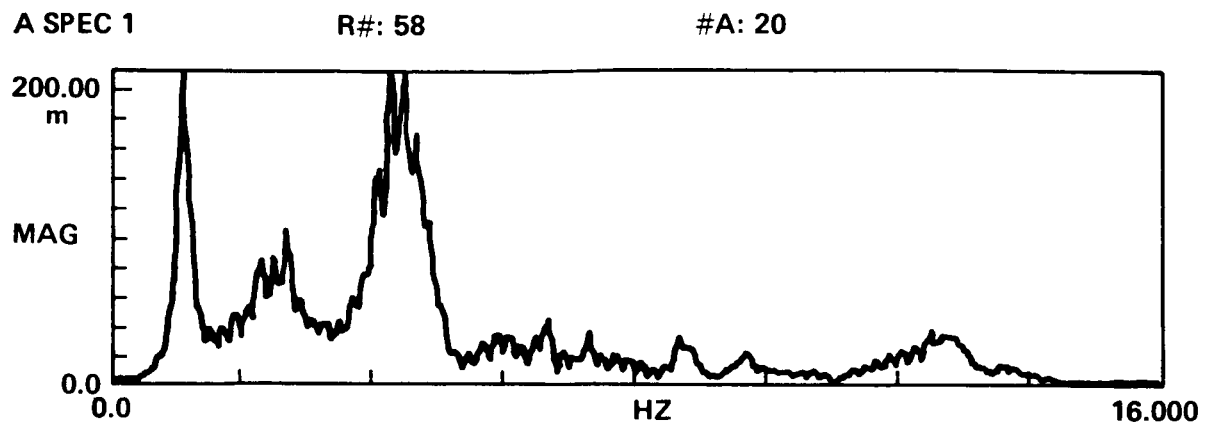


Figure 20. Open and closed loop autospectrum of Acc-A with AGS and LMED-A controller.

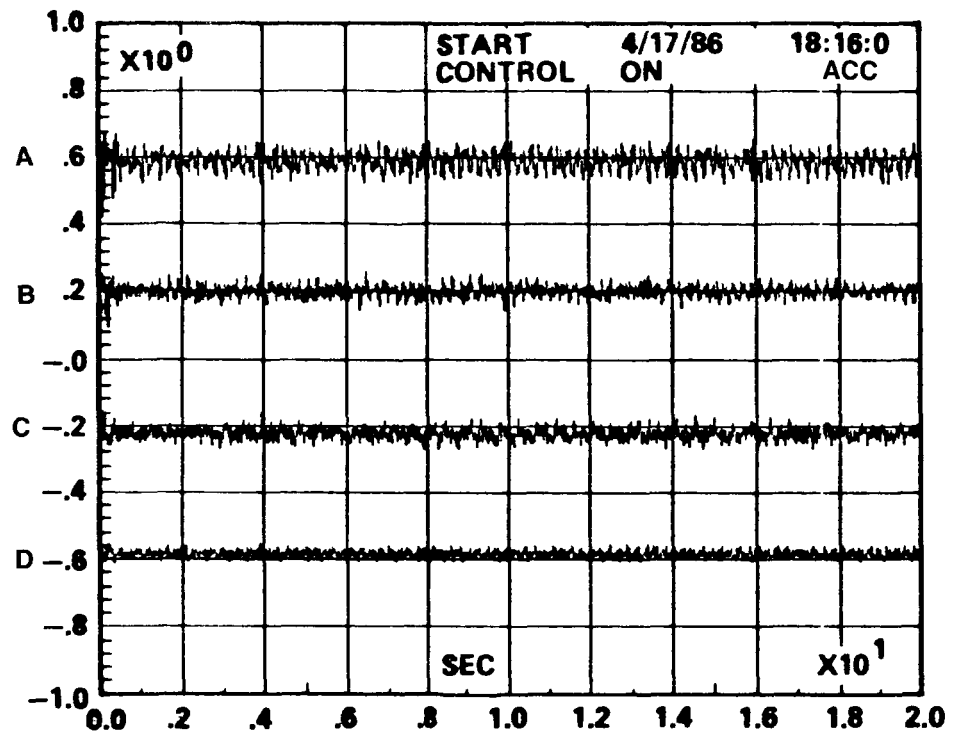


Figure 21a. Closed loop response at 4.4 Hz; LMED-A controller only.

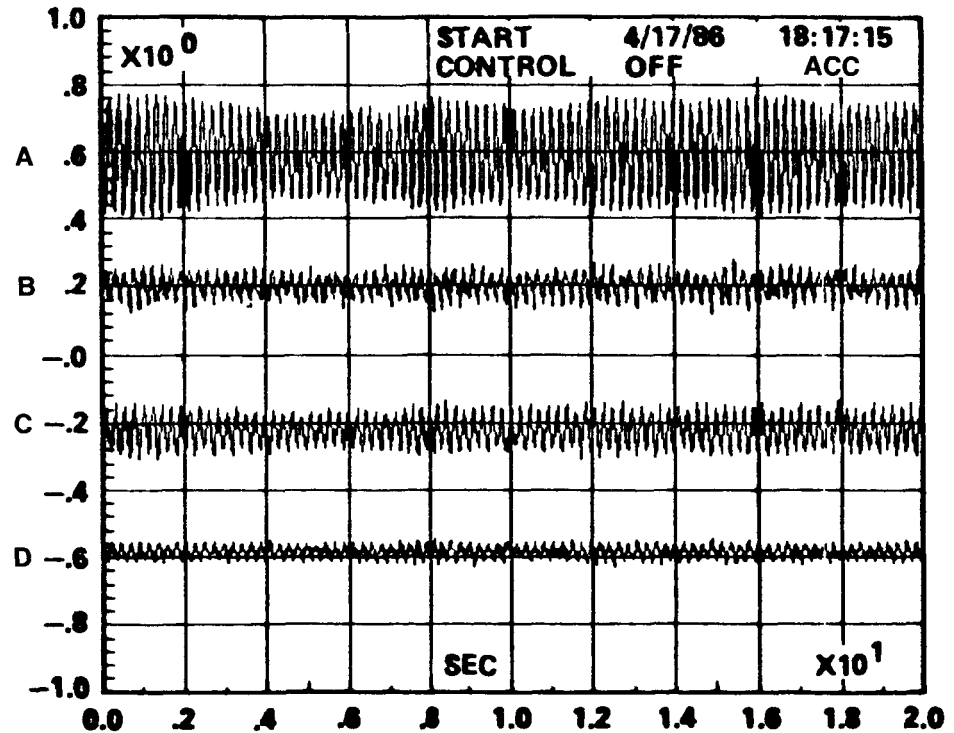


Figure 21b. Open loop response at 4.4 Hz; LMED-A controller only.

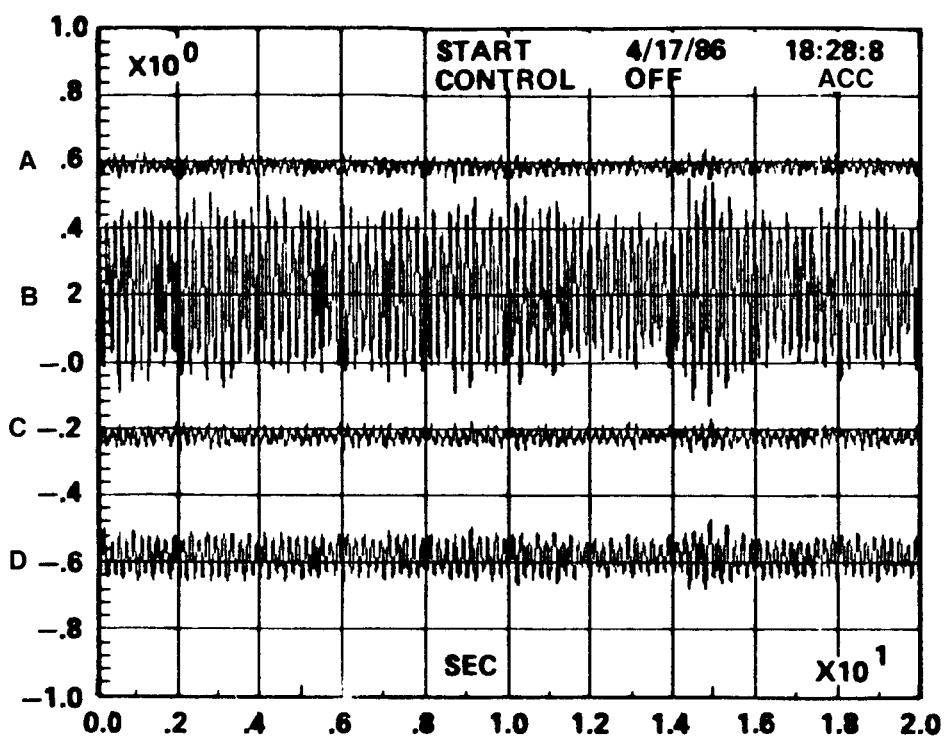


Figure 21c. Open loop response at 4.4 Hz; LMED-B controller only.

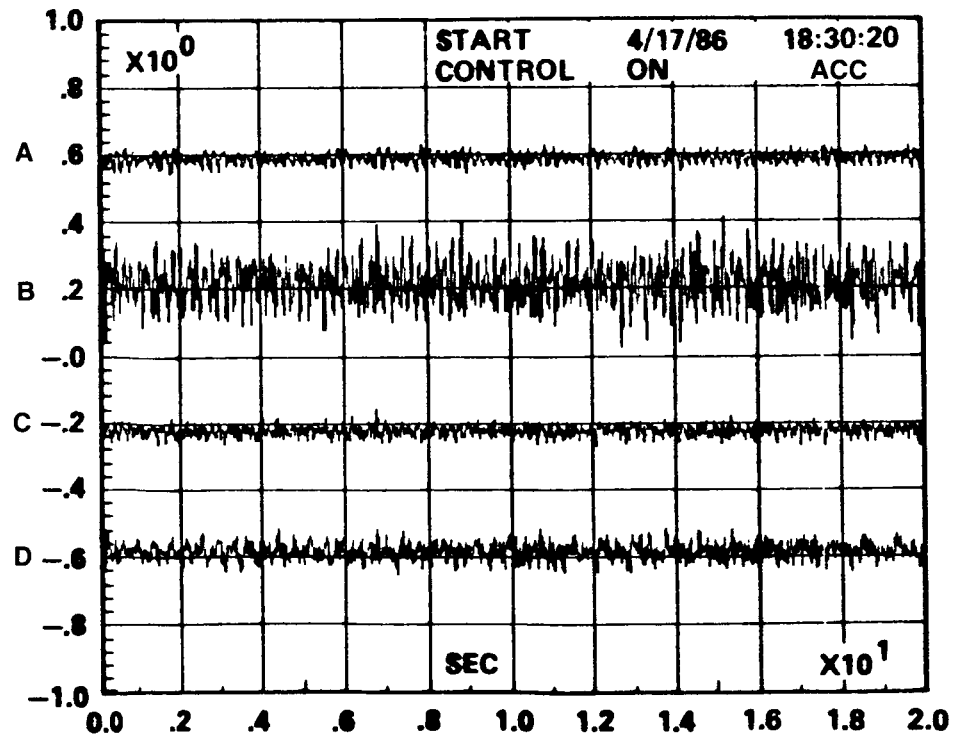


Figure 21d. Closed loop response at 4.4 Hz; LMED-B controller only.

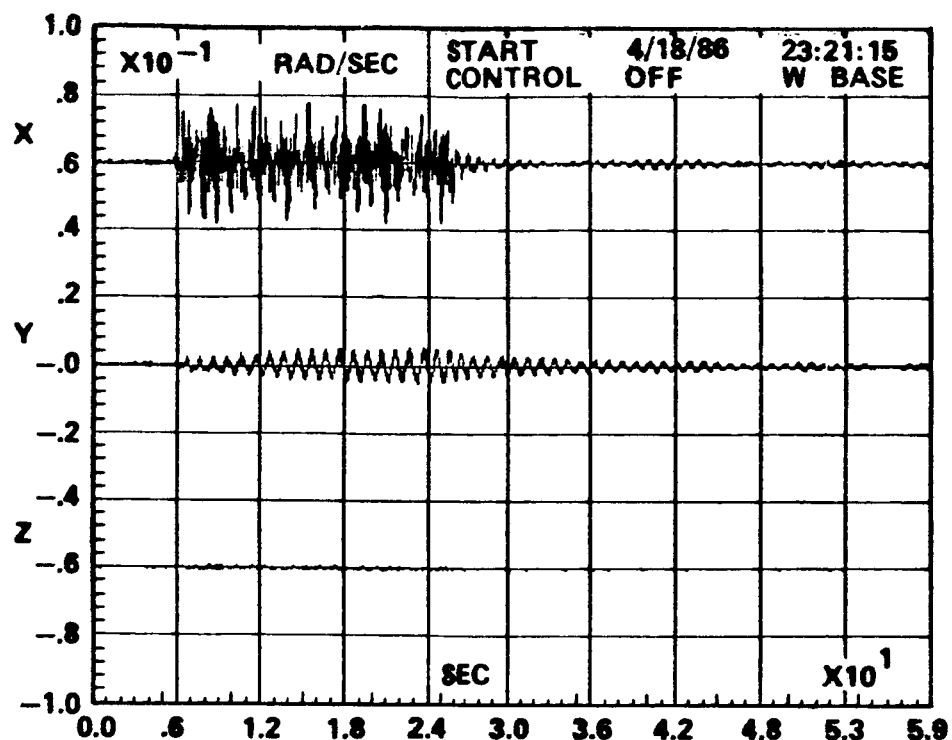


Figure 22a. Open loop response of rate gyro; BET at 1 Hz.

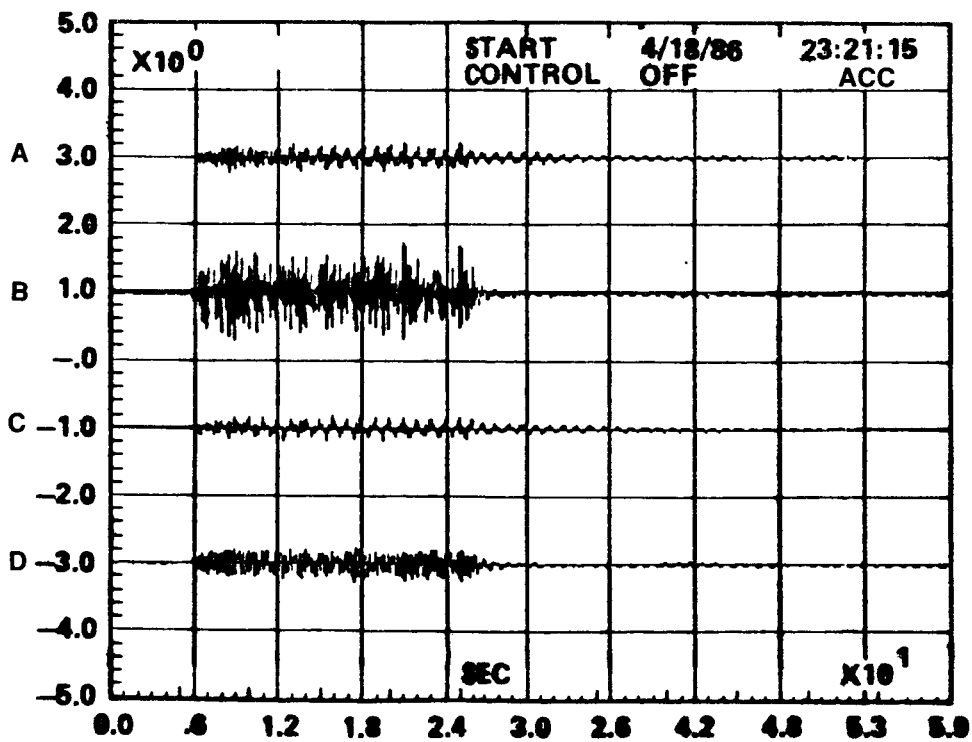


Figure 22b. Open loop response of LMED accelerometer; BET at 1 Hz.

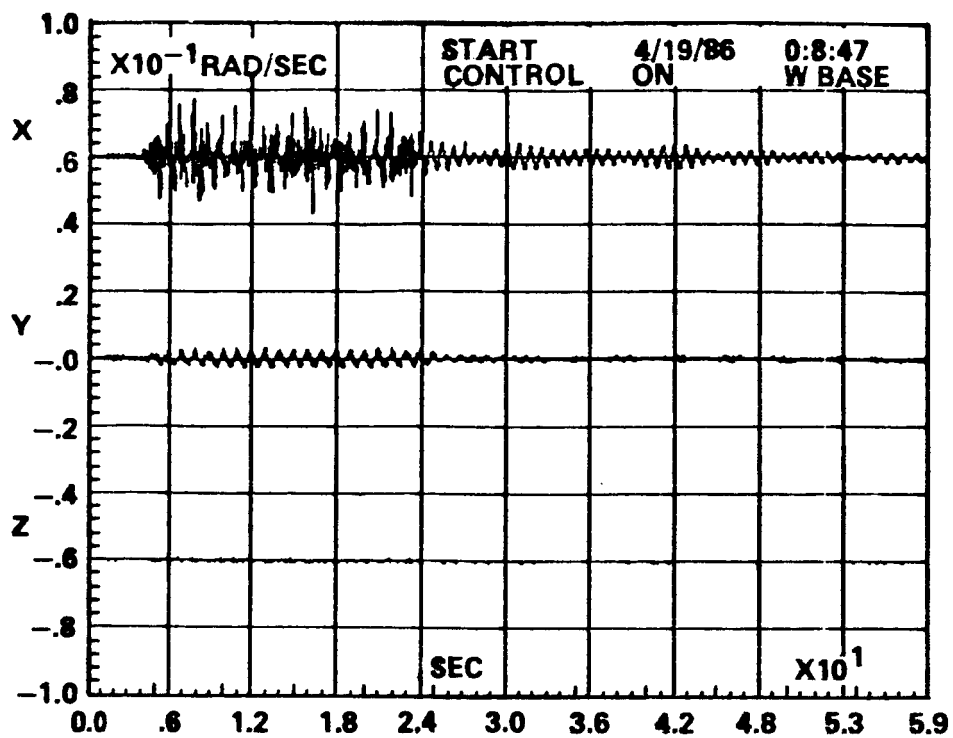


Figure 22c. Closed loop response of rate gyro with all LMEDs and AGS; BET at 1 Hz.

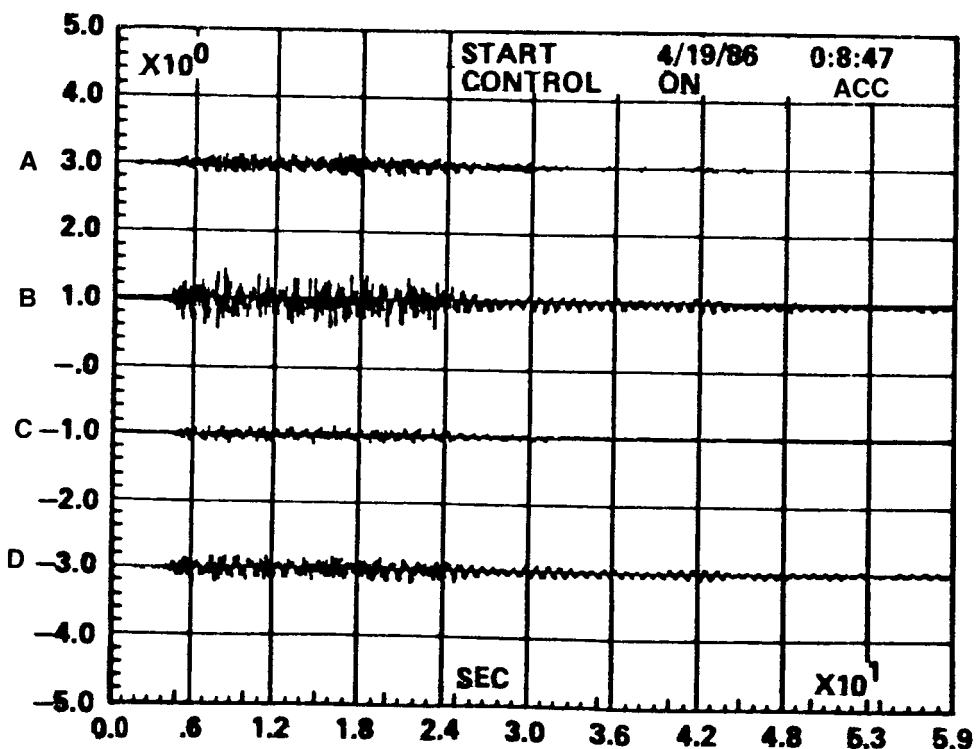


Figure 22d. Closed loop response of LMED accelerometer with all LMEDs and AGS; BET at 1 Hz.

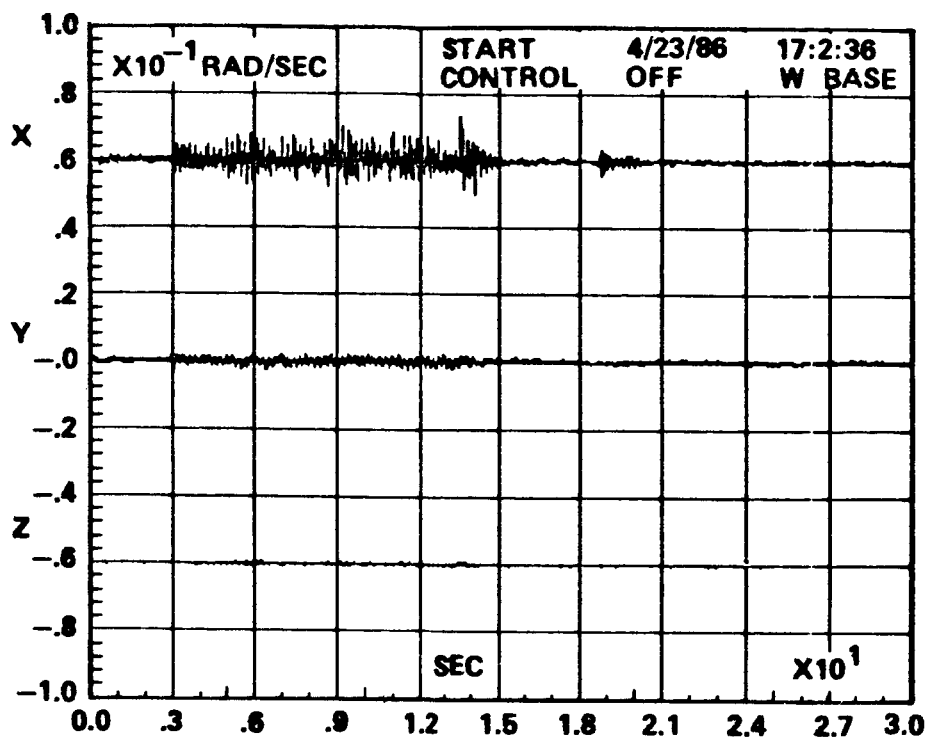


Figure 23a. Response of rate gyro at 5 Hz with all actuators except LMED-B.

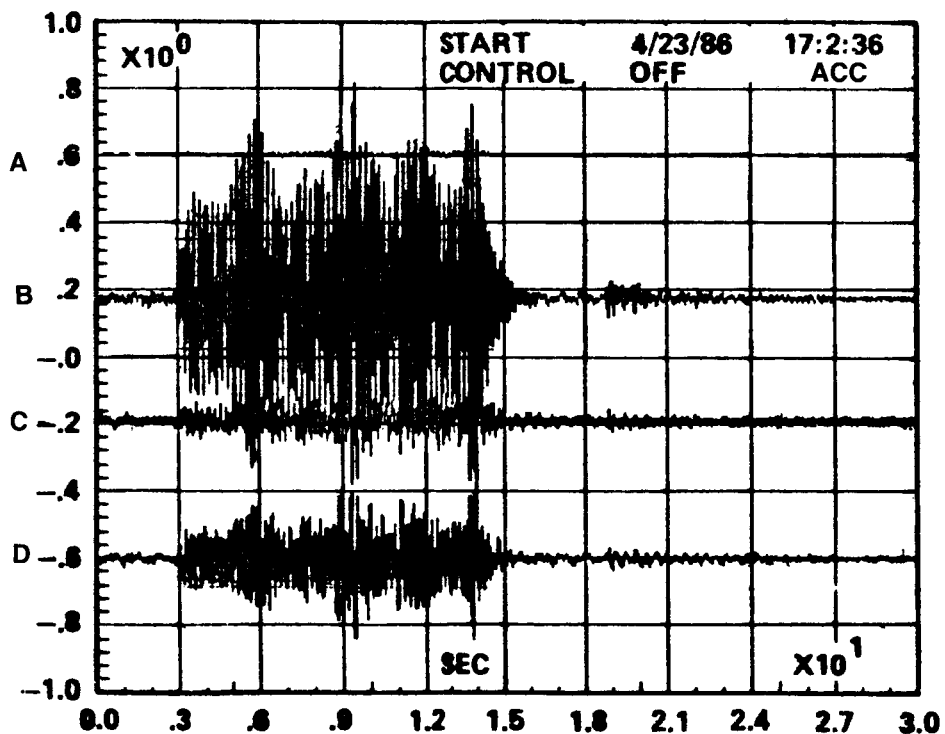


Figure 23b. Response of LMED accelerometer at 5 Hz with all actuators except LMED-B.

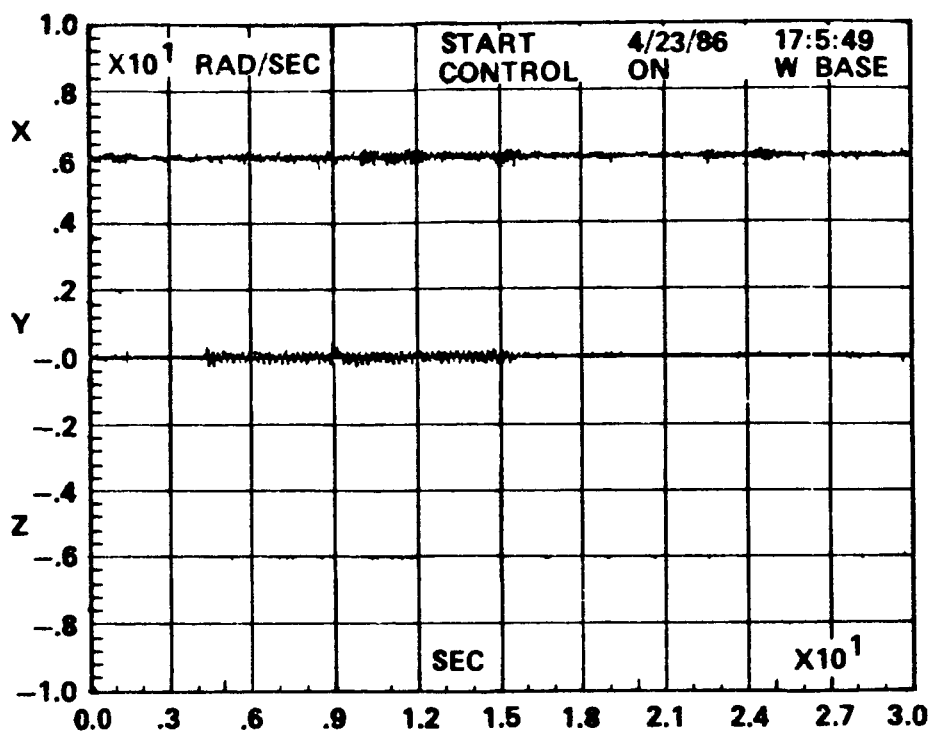


Figure 23c. Response of rate gyro at 5 Hz with all actuators operating.

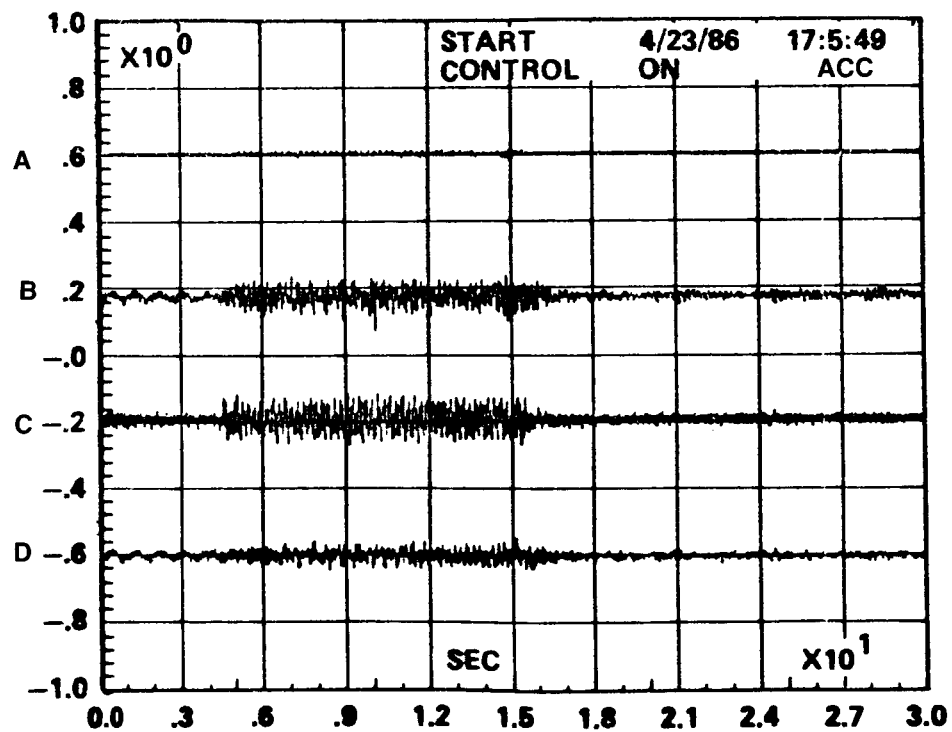


Figure 23d. Response of LMED accelerometer at 5 Hz with all actuators operating.

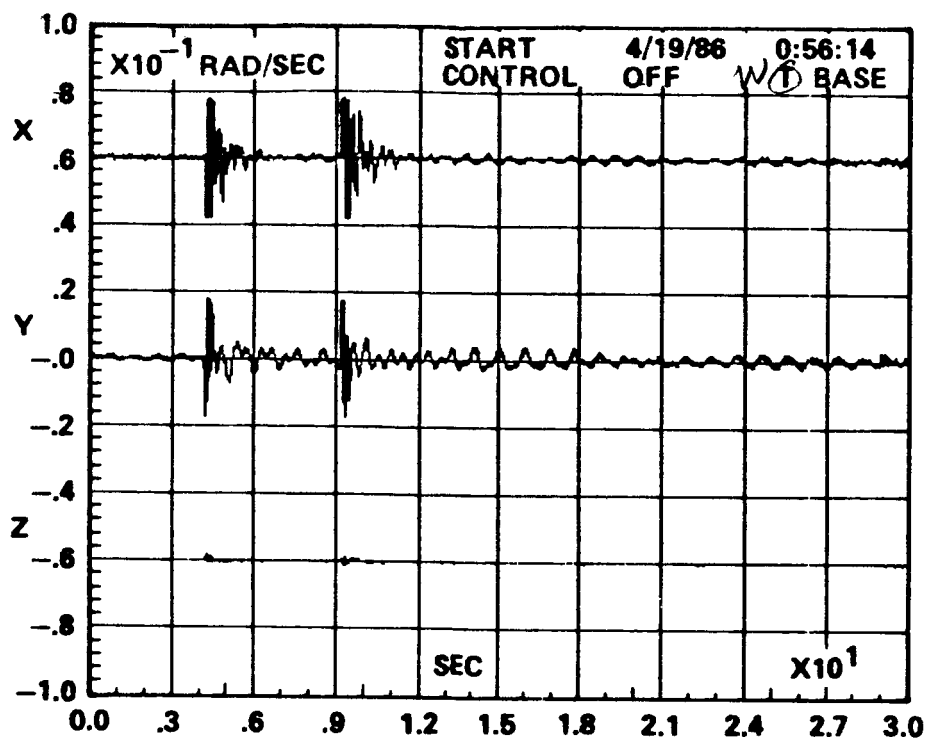


Figure 24a. Open loop transient response of rate gyro (base excitation).

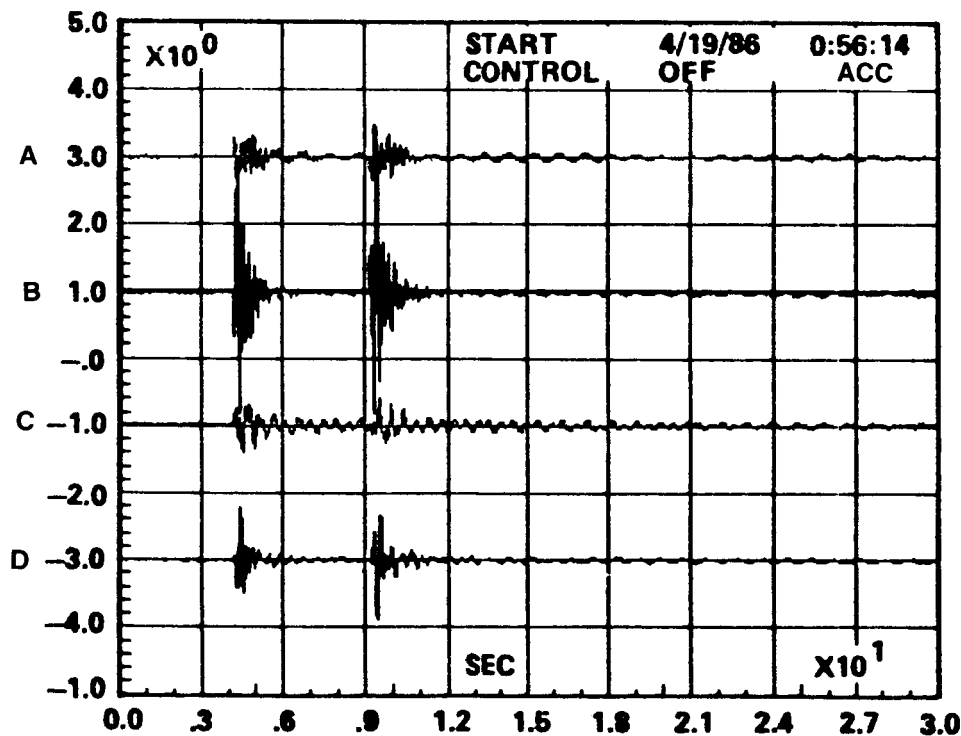


Figure 24b. Open loop transient response of LMED accelerometer (base excitation).

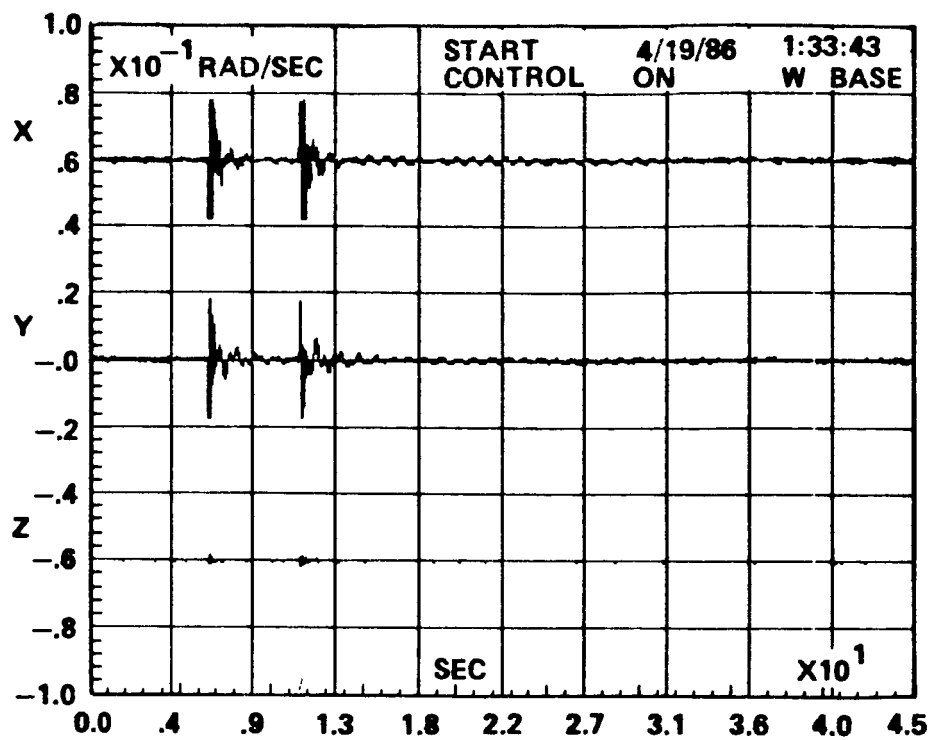


Figure 24c. Closed loop transient response of rate gyro (base excitation).

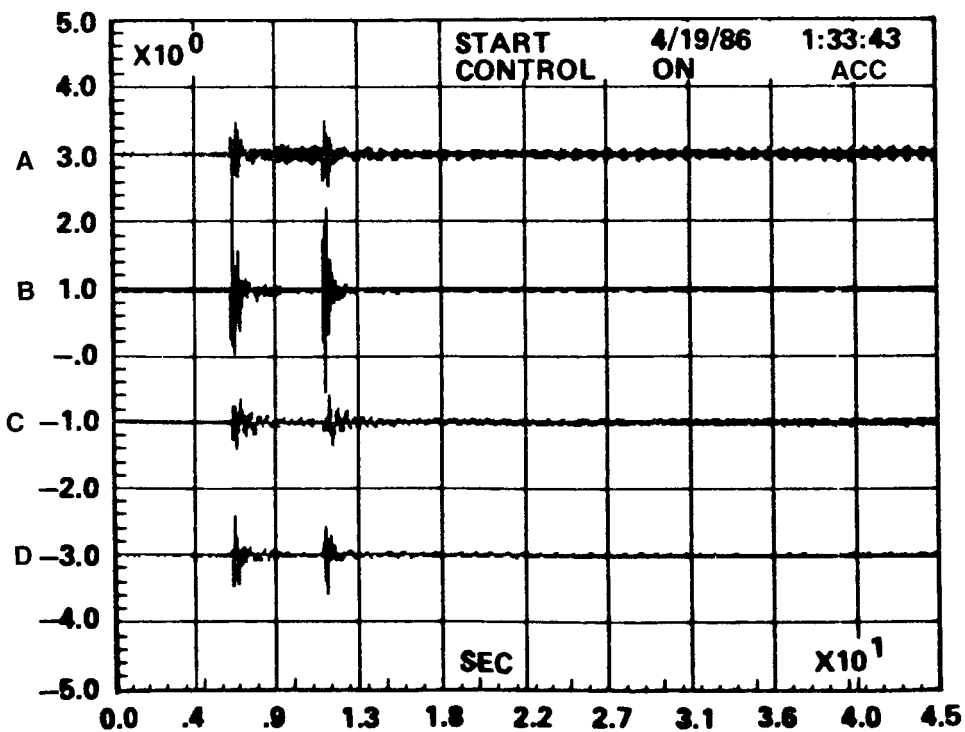


Figure 24d. Closed loop transient response of LMED accelerometer (base excitation).

3) The above comments require that a structure's open-loop frequency response be well known, either analytically or experimentally, prior to control law design with the present hardware.

4) The LMED nonlinearities, and the attendant generation of frequency harmonics, complicate the analysis of experimental results. It is not clear whether the nonlinearities or the "control spillover" is responsible for the destabilizing tendencies of the LMEDs toward the "uncontrolled" modes.

5) Although the supporting data is not presented, test data has shown that the middle LMEDs (A and C) and the AGS together achieved better vibration suppression than either system could alone, using the given forms of control algorithms.

## VI. RECOMMENDATIONS

1) The LMED hardware needs to be carefully reworked to eliminate the dominant non-linearities. Careful alignment of the linear shaft must be ensured. Furthermore, the ball bearings should be replaced with high quality, preferably non-magnetic, components. The linear shaft should be replaced with high quality non-magnetic material. The reworked LMEDs should then be carefully characterized and supported with analytic models. See the report entitled "Characterization and Hardware Modifications of LMEDs" prepared by Control Dynamics for MSFC.

2) Subsequent experiments should be planned carefully, allowing sufficient time to resolve unexpected problems which invariably occur. These experiments should include a period of thorough open-loop testing to validate analytic models.

3) The control laws developed for future tests should first be designed, tested and evaluated based on the analytic models. These algorithms could subsequently be re-tuned based on experimental results. This would be more representative of the LSS control problem, and would address the requirements for on-orbit dynamic testing and verification.

4) Detailed analytic predictions should be available to help analyze the experimental results. Such analysis might include eigenvalue and eigenvector analyses along with digital simulation capabilities. Such work was initiated at MSFC to support the VCOSS-II experiments. However, the results obtained only crudely agreed with the experimental data. This was attributed primarily to the unverified dynamic models and the unmodeled actuator nonlinearities.

APPROVAL

DISTRIBUTED CONTROL USING LINEAR MOMENTUM  
EXCHANGE DEVICES

By John P. Sharkey, Henry Waites, and George B. Doane III

The information in this report has been reviewed for technical content. Review of any information concerning Department of Defense or nuclear energy activities or programs has been made by the MSFC Security Classification Officer. This report, in its entirety, has been determined to be unclassified.

*GFM: McDonough*

---

G. F. McDONOUGH  
Director, Structures and Dynamics  
Laboratory

## TECHNICAL REPORT STANDARD TITLE PAGE

1. REPORT NO. NASA TM-100308	2. GOVERNMENT ACCESSION NO.	3. RECIPIENT'S CATALOG NO.	
4. TITLE AND SUBTITLE  Distributed Control Using Linear Momentum Exchange Devices		5. REPORT DATE October 1987	
7. AUTHOR(S) J. P. Sharkey, Henry Waites, and G. B. Doane III*		6. PERFORMING ORGANIZATION CODE	
9. PERFORMING ORGANIZATION NAME AND ADDRESS  George C. Marshall Space Flight Center Marshall Space Flight Center, Alabama 35812		8. PERFORMING ORGANIZATION REPORT #	
12. SPONSORING AGENCY NAME AND ADDRESS  National Aeronautics and Space Administration Washington, D.C. 20546		10. WORK UNIT NO.	
		11. CONTRACT OR GRANT NO.	
		13. TYPE OF REPORT & PERIOD COVERED  Technical Memorandum	
15. SUPPLEMENTARY NOTES  Prepared by Structures and Dynamics Laboratory, Science and Engineering Directorate. *Control Dynamics Company, Huntsville, Alabama.			
16. ABSTRACT  MSFC has successfully employed the use of the Vibrational Control of Space Structures (VCOSS) Linear Momentum Exchange Devices (LMEDs), which was an outgrowth of the Air Force Wright Aeronautical Laboratory (AFWAL) program, in a distributed control experiment. The control experiment was conducted in MSFC's Ground Facility for Large Space Structures Control Verification (GF/LSSCV). The GF/LSSCV's test article was well suited for this experiment in that the LMED could be judiciously placed on the ASTROMAST. The LMED placements were such that vibrational mode information could be extracted from the accelerometers on the LMED. The LMED accelerometer information was processed by the control algorithms so that the LMED masses could be accelerated to produce forces which would dampen the vibrational modes of interest. Experimental results are presented showing the LMED's capabilities.			
17. KEY WORDS  Large Space Structures Linear Momentum Exchange Device Active Vibrational Control		18. DISTRIBUTION STATEMENT  Unclassified -- Unlimited	
19. SECURITY CLASSIF. (of this report) Unclassified	20. SECURITY CLASSIF. (of this page) Unclassified	21. NO. OF PAGES 49	22. PRICE NTIS